Genes vary greatly in their propensity for collateral fitness effects of mutations

Jacob D. Mehlhoff and Marc Ostermeier*

Department of Chemical and Biomolecular Engineering, Johns Hopkins University, 3400 N. Charles St., Baltimore, MD, 21218, USA

*Corresponding author: Email: oster@jhu.edu

Competing interest statement: The authors declare no competing interests.

Abstract:
Mutations can have deleterious fitness effects when they decrease protein specific activity or decrease active protein abundance. Mutations will also be deleterious when they cause misfolding or misinteractions that are toxic to the cell (i.e., independent of whether the mutations affect specific activity and abundance). The extent to which protein evolution is shaped by these and other collateral fitness effects is unclear in part because little is known of their frequency and magnitude. Using deep mutational scanning (DMS), we previously found at least 42% of missense mutations in the *TEM-1* β-lactamase antibiotic resistance gene cause deleterious collateral fitness effects. Here, we used DMS to comprehensively determine the collateral fitness effects of missense mutations in three genes encoding the antibiotic resistance proteins New Delhi metallo-β-lactamase (NDM-1), chloramphenicol acetyltransferase I (CAT-I), and 2"-aminoglycoside nucleotidyltransferase (AadB). *AadB* (20%), *CAT-I* (0.9%), and *NDM-1 (*0.2%*)* were less susceptible to deleterious collateral fitness effects than *TEM-1* (42%) indicating that genes have different propensities for these effects. As was observed with *TEM-1*, all the studied deleterious *aadB* mutants increased aggregation. However, aggregation did not correlate with collateral fitness effects for many of the deleterious mutants of *CAT-I* and *NDM-1*. Select deleterious mutants caused unexpected phenotypes to emerge. The introduction of internal start codons in *CAT-1* caused loss of the episome and a mutation in *aadB* made its cognate antibiotic essential for growth. Our study illustrates how the complexity of the cell provides a rich environment for collateral fitness effects and new phenotypes to emerge.

Main Text:

The evolution of proteins relies on an interplay between mutations and selective pressure. Mutations with beneficial or neutral fitness effects persist, contributing to genetic diversity, while mutations with deleterious fitness effects are filtered out of the population with time. Understanding the mechanisms underlying the fitness effects of mutations is important for the study of evolution. Building on the observations that protein misfolding and misinteractions can cause deleterious fitness effects (Parsell and Sauer 1989; Krylov et al. 2003; Lemos et al. 2005; Geiler-Samerotte et al. 2011; Olzscha et al. 2011; Levy et al. 2012; Yang et al. 2012; Navarro et al. 2014; Bratulic et al. 2015), we have proposed it is useful to broadly categorize the fitness effect of mutations into two types: primary and collateral (Mehlhoff et al. 2020). Primary fitness effects are those caused by changes in the ability of the gene to perform its physiological function and arise from changes in protein activity and protein abundance. Collateral fitness effects are those that do not derive from changes in the gene's ability to perform its physiological function. Misinteractions, whether from proteins in a misfolded or natively folded state, are a likely source of deleterious collateral fitness effects. Primary and collateral fitness effects are not mutually exclusive. Mutational effects may be only primary, only collateral, or a combination of both. Knowledge of the frequency and mechanisms by which collateral fitness effects arise is essential to understanding evolutionary pathways and constraints. For example, protein misfolding and misinteractions have been proposed as reasons for the E-R anticorrelation (Zhang and Yang 2015) – the observation that protein evolution rates are best predicted by an anti-correlation with protein expression levels – but their roles continue to be debated (Biesiadecka et al. 2020; Usmanova et al. 2021; Wu et al. 2022). In addition, while collateral fitness effects are possible whenever the gene is expressed, primary fitness effects only manifest when the gene is expressed, is under selective pressure for its physiological function, and is not in a regime where fitness is buffered against the mutational effects on protein function and abundance (Mehlhoff et al. 2020).

Collateral fitness effects of mutations can be observed by growing cells in environments in which the physiological function(s) of the gene are irrelevant to organismal fitness. Studying the fitness effect of mutations in antibiotic resistance genes in environments lacking their relevant antibiotic is a convenient model system because any fitness change can be presumed to be a collateral fitness effect. We previously measured the collateral fitness effects for all single-codon missense and nonsense mutations in the antibiotic resistance gene *TEM-1* beta-lactamase (Mehlhoff et al. 2020). TEM-1 is a periplasmic protein that is exported with its N-terminal signal sequence via the Sec export pathway. Upon crossing the inner membrane during export, the signal sequence of TEM-1 is cleaved by signal peptidase I. The mature TEM-1 protein then folds via intermediates in which the α domain of the protein (residues 69 to 212) is collapsed followed by the assembly of the two lobes of the α/β domain. One surprising finding from our study was that deleterious collateral fitness effects were very common. At least 42% of missense mutations caused a 1% or greater fitness reduction. Mutations causing deleterious collateral fitness effects included signal sequence mutations that caused improper signal sequence cleavage and aggregation, mutations involving cysteine that caused incorrect intermolecular disulfides and aggregation, nonsense mutations that caused truncated proteins to aggregate, and mutations in the α domain that caused aggregation. Mutations causing deleterious collateral fitness effects caused activation of select outer-envelope stress pathways, but not all mutations activated the same pathways, suggesting different mechanisms for the deleterious effects.

We wondered if the high frequency of deleterious collateral fitness effects in *TEM-1* was typical of most genes. We also wondered if aggregation would be associated with the deleterious collateral fitness effects in other genes. Here, we report the frequency and magnitude of collateral fitness effects of mutations in three different bacterial antibiotic resistance genes native to *E. coli*. We explore the mechanistic determinants of these effects including the role of aggregation and describe unexpected phenotypes caused by some mutations.

Results

Deleterious collateral fitness effects of mutations occur less frequently in NDM-1, CAT-I, and AadB relative to TEM-1.

We expanded our study of collateral fitness effects of mutations by choosing proteins that differed from TEM-1 by quaternary structure, subcellular location, and post-translational processing. We initially identified New Delhi metallo-β-lactamase (*NDM-1*), chloramphenicol acetyltransferase I (*CAT-I*), 2”-aminoglycoside nucleotidyltransferase (*aadB*), and aminoglycoside 6’-N-acetyltransferase (*aac(6’)-Im*) as candidate antibiotic resistance genes for studying collateral fitness effects. All four genes have no known physiological functions outside of providing antibiotic resistance, making the genes superfluous during growth in the absence of antibiotic.

NDM-1 is a class B metallo-β-lactamase which has been natively found in *E. coli* as a 270-residue protein and has undergone rapid, worldwide dissemination since being first identified in 2008 (Yong et al. 2009). A metallo-β-lactamase, it evolved independently from TEM-1 and relies on two zinc ions in the active site to coordinate a nucleophilic attack of β-lactam antibiotics including penicillins, cephalosporins, and carbapenems (Zalucki et al. 2020). NDM-1 offered a periplasmic protein to compare with TEM-1. NDM-1 is reported to exist as a monomer (Guo et al. 2011) or a mixture of monomers and dimers in solution (King and Strynadka 2011). NDM-1 contains two cysteines (C26 and C208) but unlike TEM-1 does not form a native disulfide bond. Several studies have shown that it anchors to the outer membrane

following export to the periplasm via the Sec export pathway, cleavage of its signal peptide, and lipidation at C26 (González et al. 2016; Prunotto et al. 2020). However, NDM-1's categorization as a lipoprotein has been challenged (Zalucki et al. 2020).

The other three proteins were cytoplasmic proteins. Chloramphenicol acetyltransferases (CAT) provide high-level chloramphenicol resistance and are commonly divided into three types: CAT-I, CAT-II, and CAT-III (Biswas et al. 2012). Of the three variants, CAT-I is the most prevalent and native to *E. coli* (Awad et al. 2016). AadB and AAC(6') are monomeric enzymes that covalently modify aminoglycoside antibiotics at different sites (Wright and Serpersu 2005; Cox et al. 2015). CAT-I, AadB, and AAC(6') lack the potential for two types of mechanisms associated with deleterious effects in TEM-1 because cytoplasmic proteins lack export signal sequences and cannot form disulfides due to the cytoplasm's reducing environment. However, the cytoplasm offers a larger number of proteins with which these proteins might misinteract. In addition, CAT-I's homotrimer state adds oligomerization as an additional process through which collateral fitness effects might arise.

We replaced the *TEM-1* gene in pSKunk-1 with *NDM-1*, *CAT-I*, *aadB*, and *aac(6')-Im*, placing the genes under control of the isopropyl β-D-1-thiogalactopyranoside (IPTG) inducible *tac* promoter. All four genes provided the expected antibiotic resistance in cultures containing IPTG (**supplementary fig. S1A**, Supplementary Material online). With the exception of AAC(6'), expression of the antibiotic resistance proteins caused little, if any, fitness effects (**supplementary fig. S1B**, Supplementary Material online). We eliminated AAC(6') as a candidate for studying collateral fitness effects because of its large fitness cost of expression. Expression levels of wild-type NDM-1, CAT-I, and AadB were moderate and did not cause significant changes in the *E. coli* transcriptome (**supplementary fig. S2**, Supplementary Material online).

We constructed libraries designed to contain all possible single-codon substitutions in *NDM-1*, *CAT-I*, and *aadB* and transformed these libraries into NEB 5-alpha LacI^q *E. coli* cells. We used a growth competition experiment in which uninduced, exponentially growing cultures were diluted to a starting optical density (OD-600 nm) of 0.02 in lysogeny broth (LB) media. We added IPTG to induce expression and allowed the library cultures to grow for approximately 10 generations at 37°C in the presence of the plasmid maintenance antibiotic spectinomycin but in the absence of the gene's cognate antibiotic. We thereby assumed any fitness effects of mutations measured during growth competition in the absence of the antibiotic are collateral fitness effects. We used deep sequencing to determine the frequencies of wild-type and mutant alleles at the start and end of the 10 generations of growth. We also combined the counts of synonymous alleles to determine the frequencies of missense and nonsense mutations (i.e., on the amino acid level). We calculated the fitness (w) from these frequencies. In doing so, our measure of fitness corresponds to the mean growth rate of cells containing a mutant allele relative to the mean growth rate of cells containing the wild-type allele. From the collateral fitness effects, we calculated a selection coefficient, $s = w - 1.0$, for each mutation.

In two biological replicates, we measured the collateral fitness effects for 98.6% (5322/5400), 99.9% (4375/4380), and 94.9% (3359/3540) of the possible nonsynonymous mutations in *NDM-1*, *CAT-I*, and *aadB*, respectively. The apparent beneficial fitness effects of nearly all mutations (including nonsense mutations) at codons 26-28 and 132-134 of *NDM-1* and codons 155-156 of *aadB* were deemed spurious for several reasons (**supplementary text and figs. S3 and S4**, Supplementary Material online) including the fact that monoculture growth experiments for select mutations at these positions confirmed they lacked any significant fitness effect (**supplementary fig. S5**, Supplementary Material online). Deleterious collateral fitness effects occurred at a much lower frequency in *NDM-1* (0.24%), *CAT-I* (0.87%), and *aadB* (3.76%) than in *TEM-1* (21.6%) using the criteria of $P<0.01$ (Z-test) in both replicates (**fig. 1A-D**). We also estimated the percentage of missense mutations which caused more than a 1%

decrease in fitness by assuming that selection coefficients for neutral mutations will be symmetrically distributed around a selection coefficient of 0.0 and that no mutations cause beneficial collateral fitness effects. This analysis confirmed that deleterious collateral fitness effects were rare in *NDM-1* and *CAT-I*, but a significant fraction of mutations in *aadB* (20.2%) have deleterious effects of >1% by this analysis (**fig. 1E-H**).

Neither impaired signal sequence cleavage nor increased aggregation is sufficient or necessary to cause deleterious collateral fitness effects in NDM-1.

Only 0.24% (12/5057) of missense mutations in *NDM*-1 resulted in measurable deleterious collateral fitness effects in both replica experiments (P<0.01, Z-test) (**fig. 2**). Collateral fitness effects were not observed at residues H120, H122, D124, H189, C208, and H250 responsible for coordinating the zinc ions and forming the active site. We created five missense mutants of *NDM-1* that caused over a 25% reduction in fitness as measured by DMS (**fig. 2A**). We monitored the growth rate for monocultures of cells expressing these mutants relative to cells expressing wild-type NDM-1 over 10 generations of exponential growth. From the starting and final optical density (OD) of the monocultures, we calculated a mean growth rate to determine the fitness effects of these mutations (**supplementary fig. S5**, Supplementary Material online). Highly deleterious mutations as measured by DMS were confirmed to be deleterious via monoculture growth (**fig. 2C**). These mutations were at the G25 and C26 residues, positions that are likely to affect export and subsequent lipidation of NDM-1. Like other β-lactamases, NDM-1 is exported through the Sec export pathway (González et al. 2016; Cheng et al. 2018). However, NDM-1 has an atypical signal peptide and is inefficiently secreted (Zalucki et al. 2020). A canonical Sec signal peptide contains a positively charged N region, a hydrophobic core region, and a neutral C-terminal region that contains the cleavage site immediately after a consensus A–X–A motif (Auclair et al. 2012). NDM-1 has the sequence A-L-A-A-A starting at residue 16, suggesting possible cleavage by signal peptidase I after residue 18 or 20. Studies on NDM-1 with a C-terminal His-tag have identified cleavage after positions 15, 17, 18, and 35 (Thomas et al. 2011) and 21 (Zalucki et al. 2020). However, NDM-1 contains a canonical LSGC lipobox motif at the C-terminus of the signal sequence (residues 23-26), a site that would be cleaved by lipoprotein type II signal peptidase (LspA) after residue 25 (**fig. 2A**). Studies of NDM-1 with a C-terminal Strep-tag found such cleavage after position 25 (González et al. 2016; Prunotto et al. 2020). Thus, the consensus is that NDM-1 is a lipoprotein that anchors to the inner leaflet of the outer membrane in Gram-negative bacteria through C26 after cleavage by LspA (González et al. 2016; Prunotto et al. 2020). Both lipidation and a native affinity of NDM-1 toward the membrane allow the protein to anchor to the inner leaflet of the outer membrane in gram-negative bacteria. NDM-1 anchors in a stable, defined conformation with an exposed active site (Prunotto et al. 2020).

For the wild-type protein, NDM-1 appeared in the total soluble, periplasmic, and inclusion body fractions, but only a small amount appeared in the membrane fraction (**fig. 2B**). The size of the protein in all fractions suggests that it is the mature protein without a signal sequence. G25 is in the LSGC lipobox and immediately precedes the LspA cleavage site. Mutations G25C, G25S, and G25T, but not any other mutation at G25, caused large deleterious effects (**fig. 2AC**). G25C and G25S did not appreciably alter the amount or size of NDM-1 in the soluble or inclusion body fractions, and the species was detected in the periplasmic fraction (**fig. 2B).** In contrast, the G25T mutation led to a drastic reduction in levels of mature NDM-1 in the soluble and insoluble fractions and the appearance of a higher molecular weight band in both fractions, suggesting G25T disrupts regular cleavage of the signal sequence. No NDM-1 species with the G25T mutation could be detected in the periplasmic or membrane fractions.

Only C26S and C26D caused deleterious collateral fitness effects at position 26, and the effects were very large. Irregularities in the growth behavior of cells expressing these two

mutants (**supplementary fig. S10A**, Supplementary Material online) led us to discover that insertion of an IS4-like element ISVsa5 family transposase within NDM-1 would occur during the 10 generations of induced monoculture growth, complicating fitness measurements. This transposase preferentially targets 5'-GCTNAGC-3' sites (Halling and Kleckner 1982). Such a site overlaps codons 22-24 in *NDM-1* immediately preceding where the transposase insertion often took place. The transposition evidently alleviated the deleterious collateral fitness effects of these mutations by preventing NDM-1 expression. Due to C26S and C26D's large deleterious effect on growth, cells containing the transposition became a significant fraction of the population by generation 10 (**supplementary fig. S10B**, Supplementary Material online). We made synonymous mutations at residue 23 and 24 to change the sequence to 5'-GTTATCA-3' to get a truer estimate of the collateral fitness effect of the C26S and C26D mutations. These synonymous mutations greatly reduced the appearance of cells with the transposition in *NDM-1* (**supplementary fig. S10C**, Supplementary Material online). Subsequent experiments examining the effects of C26S and C26D used *NDM-1* genes with these synonymous substitutions and confirmed their large deleterious effect (s~ -0.7) (**fig. 2C** and **supplementary fig. S10D**, Supplementary Material online).

We also characterized the neutral mutations C26L and C26A (**fig. 2B**) to compare with C26S and C26D. C26A has been shown to result in soluble NDM-1 accumulating in the periplasm because it removes the lipidation site, thereby preventing membrane anchoring (González et al. 2016). This suggests mutations at C26 can disrupt signal sequence cleavage with a difference in association with the membrane. All four mutations reduced mature NDM-1 in the soluble, inclusion body, and membrane fractions to an undetectable level (**fig. 2B**). C26S caused the NDM-1 precursor to accumulate in the membrane fraction while the C26D and C26A mutations caused the precursor to accumulate in the periplasm. Although these results indicate C26S and C26D decreases precursor processing, the fact that the neutral mutation C26A does so as well suggests impaired removal of the signal sequence may not be the cause of the deleterious collateral fitness effects of C26S and C26D.

We also characterized the neutral P28A mutation because it is the sole mutation differentiating the naturally occurring NDM-2 variant from NDM-1. The mutation has been noted to result in a more canonical signal peptidase I cleavage site that improves secretion and leads to soluble, non-lipidated protein in the periplasm (Bahr et al. 2018; Zalucki et al. 2020). In contrast, we find the P28A mutation led to a reduction of NDM-1 in the soluble and periplasmic fraction, an increase of NDM-1 in the inclusion body fraction, and no evidence of a reduction in the small amount of NDM-1 in the membrane fraction. Despite the increase in aggregation, P28A did not cause deleterious collateral fitness effects (**fig. 2B**).

Deleterious and neutral CAT-I mutations result in protein aggregation.

A total of 0.87% (36/4156) of missense mutations in CAT-I caused deleterious collateral fitness effects in both replica experiments (P<0.01, Z-test) (**fig. 3A**). Collateral fitness effects were not observed at key active site residues, including S146 and H193. We constructed a set of 12 missense mutations in CAT-I, of which seven were deleterious in both DMS data sets and monoculture growth (**fig. 3B** and **supplementary fig. S5B**, Supplementary Material online). All deleterious CAT-I mutations produced wild-type levels of soluble protein, but unlike wild-type, most led to accumulation of CAT-I in the inclusion body fraction (**fig. 3B**). However, G202K, a neutral mutation tested to compare with the highly deleterious G202R, also caused aggregation despite its lack of a fitness effect. Aggregation of G202 mutants is consistent with the observed importance of a full-length α5-helix (residues 198-211) for correct folding and stabilization of CAT-I (Van der Schueren et al. 1996). Similarly, non-hydrophobic mutations at C212 have been reported to cause inclusion body formation (Van der Schueren et al. 1996), yet such substitutions did not cause deleterious collateral fitness effects (the weighted mean s was -

0.004 with a 99% confidence interval of 0.015). Thus, aggregation of CAT-I per se is not sufficient for deleterious collateral fitness effects. If aggregation of some mutants causes the deleterious effects, then it must be because the specific nature of the aggregation is deleterious, whereas other forms of aggregation are not.

Methionine substitutions at Q26, S27, A29, and Q30 led to large-magnitude deleterious collateral fitness effects in the DMS data with selection coefficients in the range of -0.20 to -0.39. We constructed S27M and Q30M for further study. Both mutations resulted in truncated and full-length versions of CAT-I in the soluble and inclusion body fractions (**fig. 3B**). We hypothesized that the truncated version originated from the mutation causing translation initiation at these sites and that the truncated protein was the cause of the deleterious effect. To test this hypothesis, we predicted the mRNA's translation initiation rate at positions 22-34 when each codon was replaced with the start codon ATG (Reis and Salis 2020). Consistent with our hypothesis, the fitness effect for methionine substitutions correlated with predicted mRNA translation initiation rates (r^2 = 0.72) (**fig. 3D**)

One deleterious mutation occurred at a residue important for trimer formation. S155 is involved in formation of the trimeric core in the CAT-I homotrimer (Goodale et al. 2020) although the residue is weakly conserved and substituted by glycine in certain CAT homologs (Biswas et al. 2012). S155R was the only missense mutation at this position with a reproducible, deleterious effect (s =-0.034 ± 0.01). It led to CAT-I aggregates in the inclusion body fraction and almost complete loss of trimer formation as monitored by native gel electrophoresis despite the monomer being present in the soluble fraction (**fig. 3B**). Several deleterious mutations (but not the G202K neutral mutation) led to the putative trimeric species running slightly faster during native gel electrophoresis. This observation suggests that these mutations altered the nature of the trimer, though the S27M and Q30M mutants' faster migration can be explained by the presence of N-terminally truncated species.

Deleterious AadB mutations cause aggregation without a reduction in soluble protein.

The *aadB* gene was more susceptible to deleterious collateral fitness effects than *NDM-1* or *CAT*-I. We found 3.76% (120/3190) of missense mutations in *aadB* resulted in measurable deleterious collateral fitness effects in both replica experiments (P<0.01, Z-test) (**fig. 4A**). These fitness effects were often small in magnitude ($\bar{s}$ =−0.029, $\tilde{s}$ =−0.020; for all deleterious mutations P<0.01). We constructed nine mutations in *aadB* and measured their fitness effect by monoculture growth assay (**supplementary fig. S5**, Supplementary Material online). Of these nine mutations, the three mutations to methionine failed to show a significant fitness effect in monoculture growth (**supplementary fig. S5C**, Supplementary Material online). We characterized the effects of confirmed deleterious mutations V6K, A96N, A102L, and D143F. Like NDM-1, wild-type AadB was found both in the soluble and inclusion body fractions (**fig. 4B**). Only D143F altered the levels of soluble AadB, surprisingly causing a substantial increase in soluble protein. All four mutations caused an increase in AadB aggregates, although not at levels proportional to the size of their respective fitness effects. D86 is proposed as the likely catalytic base in AadB with R40, H42, D44, D46, and D86 all playing a role in coordinating ATP and the necessary magnesium ions for providing aminoglycoside resistance (Cox et al. 2015). We do not find evidence of significant collateral fitness effects for mutations at these active site residues.

Select missense mutations can cause deleterious collateral fitness effects without affecting physiological function.

We examined the relationship between primary and collateral fitness effects for several mutants using a minimum inhibitory concentration (MIC) assay as a proxy for primary fitness measurements (**fig. 5A-C**). For many mutants, collateral fitness effects roughly correlated with

primary fitness effects. Cells expressing mutants with little or no collateral fitness cost tended to retain near-full antibiotic resistance, and those mutants in *NDM-1* and *CAT-I* with the most severe collateral fitness cost completely lost the ability to confer antibiotic resistance. Notable exceptions were the S155R and T172L mutations in *CAT-I*, which had much larger primary fitness effects. This differential impact on primary and collateral fitness effects is expected, even common, as it is easy to imagine how a mutation can affect catalytic activity without causing collateral fitness effects. For example, mutations at residues in and near the active site of NDM-1 often lead to a substantial loss in resistance (Sun et al. 2018), but almost all lacked a measurable collateral fitness cost in our study. The inverse case, in which mutations with substantial collateral fitness effects had little or no primary fitness effects, is less intuitive but was observed with *TEM-1* (Mehlhoff et al. 2020). For the genes studied here, mutations G25T in *NDM-1* and D143F in *aadB* had a collateral fitness cost of 23% and 32%, respectively, yet retained the wild-type ability to confer antibiotic resistance as measured by their MIC. Because G25T prevents mature protein formation (**fig. 2B**), this means that preNDM-1 with G25T possesses catalytic activity. D143F results in an increase in soluble protein (**fig. 4B**), which may help the mutant retain the ability to confer full resistance.

Deleterious AadB mutations cause an unusual antibiotic resistance phenotype

The two *aadB* mutations causing the largest deleterious collateral fitness effects, A102L and D143F, also caused an unusual and unexpected antibiotic resistance phenotype: band-pass resistance behavior (**fig. 5D**). Cells with the D143F mutation grew at kanamycin concentrations as high as 256 μg/ml, but these cells were unable to grow at any concentration of kanamycin ≤ 32 μg/ml including, remarkably, the absence of kanamycin. Similarly, cells with A102L grew on plates containing 16 or 32 μg/ml kanamycin but formed fewer colonies on plates with either lower or higher levels of antibiotic. Such band-pass behavior in antibiotic resistance has been engineered before using a synthetic gene circuit (Sohka et al. 2009). In that case, band-pass behavior was achieved by requiring that the ratio of catalytic activity to antibiotic concentration is high enough to degrade enough of the antibiotic so that the cells can grow, but not too high to reduce the antibiotic concentration below the threshold needed to induce expression of an essential gene. Perhaps the presence of sub-lethal amounts of kanamycin induces a cell response that ameliorates the deleterious collateral fitness effects caused by D143F. Alternatively, having an abundance of the substrate kanamycin may serve to stabilize AadB's folded structure through the energy of binding, preventing aggregation or misinteractions and ameliorating the deleterious collateral fitness effects present at low or no substrate.

Select stress-response pathways are activated in cells expressing deleterious mutants.

We utilized RNA sequencing (RNA-Seq) on a subset of mutations in *CAT-I*, *NDM-1*, and *aadB* to examine how the cell's transcriptome responds to mutations causing deleterious collateral fitness effects. We calculated the fold-difference in expression levels of genes from cells expressing a mutant relative to the expression levels of those genes in cells expressing the wild-type antibiotic resistance protein. We identified genes and select pathways in which mutations caused a more than two-fold change in expression with $P<0.001$ statistical significance for multiple interconnected genes or for stress pathways. We included a control consisting of a culture of cells that lacked the antibiotic resistance gene but contained the IPTG expression inducer. A comparison of this control to a culture containing the wild-type *aadB* gene showed expression of AadB had minimal effects on the transcriptome (**supplementary fig. S2C**, Supplementary Material online). For cells containing any of the three antibiotic genes, the addition of the IPTG inducer did not cause significant changes in the transcriptome except for upregulation of the *lac* operon, as expected (**supplementary fig. S2D-F**, Supplementary Material online).

We observed that mutations lacking a significant fitness effect (G202K in *CAT-I* and P28A in *NDM-1*) or mutations that were only slightly deleterious (S155R in *CAT-I*) had much fewer and smaller-magnitude effects on the transcriptome than deleterious mutations (**supplementary fig. S14**, Supplementary Material online). The most deleterious missense mutations usually led to substantial changes in transcriptome-wide expression. However, even though G202R in *CAT-I* (s = -0.38) was slightly more deleterious than the A102L and D143F mutations in *aadB*, the *aadB* mutations caused changes in expression eight times more frequently than G202R (5.3% for G202R vs. 37.8% and 42.6% for A102L and D143F, respectively). In fact, the *aadB* mutations so perturbed the transcriptome that it was difficult to identify changes to focus on. We instead focus our discussion on the effects of *CAT-I* and *NDM-1* mutations in comparison with our previous results with *TEM-1*.

We previously showed that deleterious mutations in *TEM-1* strongly activated two periplasmic stress pathways: the phage shock protein (Psp) response and the regulator of colanic acid capsule synthesis (Rcs) pathway, with the exception that most deleterious signal sequence mutations did not activate the Rcs response despite causing some of the largest collateral fitness effects. The Psp response is believed to be induced by inner membrane stresses and may work to mitigate secretin toxicity or problems stemming from increased inner membrane permeability (Flores-Kim and Darwin 2016). In contrast, the Rcs pathway is commonly induced by outer membrane or peptidoglycan layer stresses along with disruption of periplasm functions. It triggers positive regulation of capsular polysaccharides for biofilm formation and negative regulation of motility (Wall et al. 2018).

Here, we find that deleterious mutations in NDM-1, which are at the proposed signal sequence cleavage and lipidation sites, activated both pathways (**fig. 6AB**). Like TEM-1, NDM-1 contains a signal sequence and requires export to the periplasm for folding and function. Deleterious mutations surrounding the proposed signal peptidase cleavage site in NDM-1 caused 6- to 142-fold upregulation of genes corresponding to the Psp stress response ($P<10^{-14}$). Because G25T, C26S, and C26D completely prevented mature protein formation, they may disrupt typical export across the inner membrane or signal sequence cleavage, causing deleterious collateral fitness effects leading to the activation of the Psp pathway. In agreement with that hypothesis, no deleterious mutation in the cytoplasmic proteins CAT-I or AadB activated the Psp pathway (**fig. 6A**). However, G25C and G25S did not alter the amount of NDM-1 that was correctly exported and cleaved, suggesting these mutations must activate the Psp stress pathway via a different mechanism.

Signal sequence mutations in NDM-1 but not TEM-1 activated the Rcs pathway, a difference that may result from NDM-1 being a lipoprotein that anchors to the outer membrane while TEM-1 is not. However, certain mutations in both cytoplasmic proteins caused upregulation of the Rcs pathway (A102L and D143F in *aadB* and, to a lesser extent, G202R in *CAT-I*) (**fig. 6B**). This suggests that mutational consequences in the cytoplasm can cascade to activate the Rcs pathway.

Like *TEM-1*, deleterious mutations in *NDM-1* did not cause activation of two other periplasmic stress responses (σ^E and BaeR) but did show mild activation of the Cpx envelope response (**supplementary fig. S15A**, Supplementary Material online). The Cpx envelope stress-response is thought to help retain inner membrane integrity and is stimulated by inner membrane stress as well as misfolded inner membrane or periplasmic proteins (Raivio 2014; Grabowicz and Silhavy 2017). The S27M and Q30M methionine substitutions in *CAT-I* along with the highly deleterious *aadB* mutations caused a slight upregulation of genes in the σ^H-mediated heat shock response (**supplementary fig. S15B**, Supplementary Material online).

All five highly deleterious *NDM-1* mutations caused changes in gene expression indicative of periplasmic oxidative stress (**fig. 6C**). First, the expression of *soxS* and its paralog, *marA,* were elevated 3- to 15- fold ($P<10^{-15}$) and 4- to 27-fold ($P<10^{-11}$), respectively. Both encode transcriptional activators that regulate an overlapping set of genes, with SoxS helping in

the removal of superoxide and MarA helping in resistance to antibiotics (Holden and Webber 2020). The increased expression of these activators did not result in changes in expression of most of their target genes except for a 3- to 6- fold reduction in *ompF* ($P<10^{-15}$), which encodes an outer membrane porin and a 2- to 3- fold increase in *mdtK* ($P<10^{-4}$), which encodes a multidrug efflux transporter. The second indicator of oxidative stress was an upregulation of the cysteine/cystine shuttle system, which plays an important role in oxidative stress tolerance by providing reducing equivalents to the periplasm (Mironov et al. 2020). In the system, hydrogen peroxide in the periplasm is removed in the oxidation of cysteine to cystine. Cystine is imported to the cytoplasm via TcyP (3- to 12-fold increase in expression, $P<10^{-8}$). In the cytoplasm, cystine is reduced to cysteine so it can be shuttled back to the periplasm to remove more hydrogen peroxide. Consistent with a need for more cysteine, which is synthesized from serine and hydrogen sulfide, most genes in the *cysDNC and cysJIH* pathway for converting sulfate to hydrogen sulfide and the *cysPUWA* operon for importing sulfate/thiosulfate were upregulated in the NDM-1 mutants. The third indicator of oxidative stress was the upregulation of genes for the synthesis of enterobactin, which aside from its role in iron uptake also plays a role in the oxidative stress response (**supplementary fig. S15C**, Supplementary Material online) (Peralta et al. 2016). The cytoplasmic oxidative stress regulator *oxyR* and the genes OxyR activates when the cytoplasm experiences oxidative stress due to hydrogen peroxide did not show elevated expression.

Mutations lacking collateral fitness effects can nonetheless cause specific changes in gene expression

Interestingly, we observed that a mutation without a collateral fitness effect could cause a precise and large change in gene expression. Both G202R and G202K cause CAT-I aggregation yet only G202R causes a collateral fitness effect (s = -0.38 ± 0.01 and 0.01 ± 0.01, respectively). Surprisingly, both mutations (but not the other three CAT-I mutations) caused a dramatic increase in *agn43* expression (18- and 29-fold, respectively, $P<10^{-15}$), a gene that encodes two outer membrane proteins (**fig. 6C**). Both mutations also caused a similar expression increase in *yeeRS* immediately downstream. Expression of *agn43* is blocked by binding of OxyR to the *agn43* promoter (independent of OxyR's oxidative state), but *dam* methylation of the *agn43* promoter blocks OxyR binding. Competition between Dam and OxyR determine *agn43* expression (Kaminska and Van Der Woude 2010). Because neither *dam* nor *oxyR* expression was altered by the mutations, the mutations may cause CAT-I to interfere with OxyR binding, perhaps via aggregation, causing high *agn43* expression. Ag43 has been linked to the oxidative stress response and biofilm formation (Laganenka et al. 2016).

Mutations at the same position can cause opposite changes in gene expression

We observed one instance in which two mutations at the same position caused opposite changes in expression of a stress response pathway. Many deleterious mutations across all four antibiotic resistance genes caused a decrease in expression of *gadE*, *gadX*, and *gadW*, as well as a repression of genes activated by GadX/GadW as part of the glutamate-dependent acid resistance response (Tucker et al. 2003), which helps restores pH homeostasis in acidic environments (**fig. 6D**). However, the G25C mutation in *NDM-1* caused activation of the acid resistance response with a 10- to 23-fold increase in expression of *gadA* and *gadBC* ($P<10^{-15}$), in sharp contrast to G25S and G25T. GadA and GadB catalyze the H^+-consuming conversion of glutamic acid to γ-aminobutyrate (De Biase et al. 1999). Neither G25C nor G25S alter the fate of NDM-1 (**fig. 3B**) and otherwise produce very similar changes to the transcriptome. Because Cys and Ser only differ by one atom (sulfur vs. oxygen), this suggests that it is the reactivity of a cysteine in the G25C mutation that causes the differential activation of the glutamate-dependent acid resistance response.

S27M and Q30M mutations in CAT-I cause loss of the episome

We observed the S27M and Q30M methionine substitutions in *CAT-I* caused a dramatic decrease in expression of conjugation genes on the episome (**supplementary fig. S15D**, Supplementary Material online). In fact, both mutations caused a drastic reduction in counts for almost all episomal genes, often reducing the counts to zero (**fig. 7A**). In addition, *lacI* expression decreased 5- to 11-fold. LacI is encoded on the chromosome and the episome and represses our antibiotic genes' transcription in the absence of inducer. Suspecting the mutations might be causing loss of the episome, we used a purification method designed for isolation of large DNA molecules, performing the extraction after 10 generations of induced monoculture growth for the three most deleterious mutations in CAT-I, including S27M and Q30M. PCR amplification of the *traJ* and *traI* episomal genes from this fraction revealed the reduction or complete loss of the episome from cells expressing S27M and Q30M but not for G202R (**fig. 7B,C**). TraJ is the master regulator of *tra* operon transcription while TraI is a relaxase responsible for the beginning of the conjugation process. The most straightforward potential mechanism is that the CAT-I protein fragments resulting from the S27M and Q30M mutations interfere with episome replication, maintenance, or segregation during cell division, causing a reduction in episome propagation. Alternatively, the fragments might interact with an episomal protein such that the presence of the episome becomes toxic, resulting in selection against episome-containing cells.

Discussion

Our study shows that genes have different propensities to exhibit collateral fitness effects. What are the origins of these differences? One possible explanation is differences in a protein's propensity for aggregation/misfolding. All the deleterious mutants studied in *TEM-1* and *aadB* increased aggregation, and these two genes had the highest frequency of mutations with deleterious fitness effects. This correspondence is consistent with the hypothesis that a protein's propensity for aggregation predicts the frequency of deleterious collateral fitness effects. However, our study shows that not all aggregation causes deleterious fitness effects. Unmutated NDM-1 aggregates, and the only NDM-1 mutation studied that increased aggregation (P28A) had neutral fitness effects (**fig. 2**). G202R and G202K in CAT-I cause approximately the same amounts of aggregation, but only G202R was deleterious (**fig. 3**). For mutants of CAT-I and AadB, there was little correlation between the magnitude of the deleterious fitness effect and the amount of aggregation (**figs. 3** and **4**). The aggregation we observed cannot be deleterious to fitness due to a resource cost because then the magnitude of the effect and the amount of aggregate should positively correlate, and such a resource cost would be very small relative to the fitness effects measured here. Instead, for aggregation/misfolding to be deleterious for fitness, the aggregate/misfolded protein must misinteract with a cellular component or process in a manner that is deleterious for fitness. For example, perhaps G202R aggregates in a toxic way but G202K does not.

This perspective is important when evaluating evidence addressing the role aggregation/misfolding may play in the ER anticorrelation. Agozzino and Dill's theoretical treatment found that protein evolutionary rates are faster for less stable proteins (Agozzino and Dill 2018). In contrast, Usmanova et al. found that experimental measures of protein stability and melting temperature do not correlate with evolutionary rate (Usmanova et al. 2021). The authors interpreted this lack of correlation as undermining the argument that misfolding plays a major role in the ER anticorrelation. However, their interpretation is based on the premise that less stable proteins will be more likely to aggregate upon mutation because their stability buffer is small. However, most proteins are marginally stable (Taverna and Goldstein 2002), virtually all proteins have folding intermediates, and folding and misfolding in the cell is a kinetic

competition (Jahn and Radford 2008). Although destabilization via mutation will increase the population of partially folded conformations, the key for aggregation is how the mutations affect the nature of those intermediates and the barriers that must be overcome for the folding protein to progress to aggregation. Thus, what may be important is not just whether the mutation can sufficiently compromise the global stability of the native state, but how the mutation affects the kinetics of aggregate formation versus native folding and, most certainly, whether the aggregates interact with other cellular components to cause deleterious fitness effects.

An additional potential reason for the differences between genes in the frequency of collateral fitness effects is that chaperones and stress-response pathways likely have different abilities to alleviate the deleterious effects of mutations for the different proteins. For example, the cell's chaperones and stress responses may be more capable of buffering the negative effects caused by CAT-I and NDM-1 mutations than those caused by TEM-1 and AadB mutations. Consistent with this theory, proteins that interact with chaperones in yeast have been noted to evolve more quickly than proteins that do not (Alvarez-Ponce et al. 2019).

Given the prevalence of mutants causing aggregation, we find it curious that we observed only mild activation of two of the stress-response pathways known to respond to protein aggregation. Instead, the most commonly activated stress responses are two outer-envelope stress pathways: the Psp response induced by mutants of the periplasmic proteins and the Rcs response induced by most mutants in *TEM-1*, *NDM-1*, and *aadB* (and G202R in *CAT-I*). It is unknown whether these stress-response pathways alleviate some of the deleterious fitness effects or whether deleterious fitness effects are brought on by the useful or errant induction of these or other pathways.

We previously proposed that deleterious collateral fitness effects may play a role in protecting against genetic drift toward mutations that would otherwise compromise the protein's ability to perform its physiological function (Mehlhoff and Ostermeier 2020). Our MIC assays on select mutations with deleterious collateral fitness effects (**fig. 5**) provide only a small snapshot of the overlap of primary and collateral fitness effects in CAT-I, NDM-1, and AadB. Mutations with large deleterious collateral fitness effects also caused deleterious effects in the presence of antibiotic. In environments in which a protein is not under selection or where primary fitness effects are buffered by excess in expression or activity, deleterious collateral fitness effects will prevent the accumulation of mutations with deleterious primary effects, with fitness benefits if the gene were to later come under selection for its physiological function.

Our study provides several examples illustrating how the cell is a complex molecular space that is rich with the potential to interact with mutations in unexpected ways, altering fitness but also causing new phenotypes to emerge. The S27M and Q30M mutations in CAT-I cause loss of the episome – a normally stable extra chromosomal element. In NDM-1, G25C activates but G25S represses the glutamate-dependent acid resistance response. And most strikingly, D143F in AadB makes kanamycin, the antibiotic AadB inactivates, essential for growth. The interactions between mutations and the cell are both an evolutionary constraint and an evolutionary opportunity.

There are several lines of research that would further our understanding of the mechanisms of collateral fitness effects, the factors governing a gene's susceptibility to them, and the causes and roles of changes in gene expression. One is to use biochemical techniques to identify the biomolecules that interact with or are directly affected by the mutant proteins. Another is to examine how collateral fitness effects are impacted by the environment. For example, protein aggregation is typically lowered by reducing the growth temperature or slowing the growth rate by using a minimal growth media. Do those environmental changes also reduce collateral fitness effects? Specific to NDM-1, we studied the protein in the zinc-rich environment of LB-media. However, evidence suggests that zinc deprivation, and not enzymatic function, is the primary selective pressure acting on the evolution of NDM variants (Bahr et al. 2018). A

study of collateral fitness effects in a zinc-limited environment may provide better insight into the collateral fitness effects of mutations under more evolutionarily relevant conditions. A third approach is a genetic one. How do collateral fitness effects depend on the strain of bacteria? Does genetically removing the ability of a cell to activate a stress pathway alter the magnitude of a collateral fitness effect? Does overexpression of chaperones lessen the fitness effects? A fourth approach is to investigate the role of protein expression level. A DMS study conducted in yeast on the green fluorescent protein found at least 42% of the collateral fitness effects caused by single-nucleotide mutations in the protein were dependent on expression level (Wu et al. 2022). They found similar expression-dependent effects in a conditionally essential gene and concluded that increased expression levels in non-essential genes tended to exacerbate deleterious collateral fitness effects. However, their analysis indicated that <6% of the variability in fitness could be explained by misfolding, misinteractions, or translation errors, but that may reflect the accuracy of their measurements and predictions given the small fitness effects they observed (Wu et al. 2022).

Materials & Methods

Plasmid construction and general growth conditions.
The *TEM-1*, *NDM-1*, *CAT-I*, *aadB,* and *aac(6')-Im* antibiotic resistance genes were individually placed under control of the IPTG-inducible *tac* promoter on pSKunk1, a minor variant of plasmid pSKunk3 (AddGene plasmid #61531) (Firnberg and Ostermeier 2012). The *CAT-I* gene was amplified from pKD3 (AddGene plasmid #45604). An A to C mutation was made at base pair 219 within the *CAT-I* gene using the QuickChange Lightning Site-Directed Mutagenesis kit (Agilent) to match the native *E. coli CAT-I* sequence. The *NDM-1, aadB*, and *aac(6')-Im* genes were ordered as gene fragments with adapters from Twist Bioscience. We verified the correct size and antibiotic resistance gene sequence for each plasmid using agarose electrophoresis gels and Sanger sequencing, respectively before transforming the resulting plasmids into electrocompetent NEB 5-alpha $LacI^q$ cells. We produced these electrocompetent cells starting from a single tube of NEB 5-alpha $LacI^q$ chemically competent cells. Chemically competent cells were plated on LB-agar containing 10 µg/ml tetracycline. A single colony was selected to produce electrocompetent cells with aliquots of the resulting electrocompetent cells used for all experiments within this study. All growth experiments were conducted in LB media supplemented with glucose (2% w/v) and spectinomycin (50 µg/ml) except where otherwise noted. Expression of the antibiotic resistance proteins was induced by addition of 1 mM IPTG to exponentially growing cultures.

Library creation.
We constructed libraries of all the possible single-codon substitutions in *NDM-1*, *CAT-I*, and *aadB* using inverse PCR with mutagenic oligonucleotides as described in previous work (Mehlhoff and Ostermeier 2020). The oligonucleotides contained a NNN degenerative codon targeted to each codon within the three genes. We constructed the library in three regions for *NDM-1*, three regions for *CAT-I*, and two regions for *aadB* due to read length constraints of Illumina MiSeq. We estimated a minimum of 50,000 transformants would be necessary for each region to have a high probability of having nearly all possible single-codon substitutions (Bosley and Ostermeier 2005). For each region, we repeated the transformation and pooled the resulting colonies until we had an excess of 100,000 transformants. We recovered each library from the LB-agar plates using LB media and glycerol before making aliquots for storage at -80°C.

Growth competition for measurements of fitness effects.
Fitness was measured as described in Mehlhoff *et al.* (Mehlhoff et al. 2020) using a growth competition experiment. Our experiment differed only at the start. Frozen library stocks and wild-type cells were thawed on ice before 50 µl was added to 100 ml media containing 50 µg/ml spectinomycin and 2% w/v glucose in a 500 ml unbaffled shake flask. The cultures were incubated with shaking for 16 hours at 37°C. The wild-type and library cultures were then diluted to an of OD of 0.050 in 100 ml of media and mixed at a ratio of 2:98 based on volume in a fresh unbaffled flask. The cultures were incubated at 37°C with shaking until the OD was about 0.5 and the remainder of the growth competition followed as described in previous work. In short, the exponentially growing library cultures were induced with IPTG and allowed to grow for approximately ten generations with a single dilution at about five generations. Plasmid DNA was collected from before induction and after 10 generations of growth. Custom adapters were added to the plasmid DNA by PCR. Adapters were designed to be compatible with the Illumina platform and contained barcodes for identification of each timepoint and sample. Proper DNA size of the PCR products was validated by agarose electrophoresis gel before the PCR products were pooled and submitted for Illumina MiSeq (2 x 300 bp reads) at the Single Cell and Transcriptomics Core facility at Johns Hopkins University.

Deep sequencing analysis.
Output files from Illumina MiSeq were first run through FastQC (Andrews et al. 2018) to check read quality. The paired-end reads were merged using PEAR (Stamatakis et al. 2014) set to a minimum assembly length of 150 base pairs reads allowing for high quality scores at both ends of the sequence. Adapters were trimmed from the ends of the antibiotic resistance genes' coding sequence using Trimmomatic (Bolger et al. 2014). Enrich2 (Rubin et al. 2017) was used to count the frequency of each allele for use in calculating selection coefficients and associated statistical measures. We set Enrich2 to filter out any reads containing bases with a quality score below 20, bases marked as N, or mutations at more than one codon.

Fitness of an allele (w_i) was calculated from the enrichment of the synonyms of the wild-type gene (ε_{wt}), the enrichment of allele *i* (ε_i) and the fold increase in the number of cells during the growth competition experiment (*r*) as described by Equation 1. We utilize the frequency of wildtype synonymous alleles as the reference instead of the frequency of wildtype because wildtype synonyms occurred more frequently in the library and wildtype sequencing counts are more prone to being affected by the artifact of PCR template jumping during the preparation of barcoded amplicons for deep-sequencing. Detailed derivations of the following equations (Equations 1-6) can be found in our previous work (Mehlhoff et al. 2020).

$$w_i = \frac{\ln(r\varepsilon_i)}{\ln(r\varepsilon_{wt})} \quad (1)$$

We calculate the variance in the fitness as

$$\sigma_w{}^2 = w_i{}^2 \left[\frac{\frac{(1-f_{if})}{c_{if}} + \frac{(1-f_{io})}{c_{io}}}{(\ln r\varepsilon_i)^2} + \frac{\frac{(1-f_{wtf})}{c_{wtf}} + \frac{(1-f_{wto})}{c_{wto}}}{(\ln r\varepsilon_{iwt})^2} \right] \quad (2)$$

Where the frequency of allele (f_i) is calculated from counts of that allele (c_i) and the total sequencing counts (c_T).

$$f_i = c_i/c_T \quad (3)$$

From the variance in fitness, we calculated a 99% confidence interval. Additionally, we calculated a *P*-value using a 2-tailed test. Details of the Z-score and *P*-value equations are available in Mehlhoff *et al*. (Mehlhoff et al. 2020).

We estimated the number of false positives that would be included at $P<0.01$ and $P<0.001$ significance in order to correct for multiple testing (Storey and Tibshirani 2003) in our DMS datasets as described previously (Mehlhoff et al. 2020). For *TEM-1*, we estimated that our data would contain approximately 55.0 false positives on average at $P<0.01$ significance and an estimated 5.6 false positives on average at $P<0.001$ significance for a single replica (Mehlhoff et al. 2020). Those values are 44.1 and 4.3 (*CAT-I*), 52.8 and 5.3 (*NDM-1*), and 33.8 and 3.4 (*aadB*) at $P<0.01$ and $P<0.001$ significance, respectively. We chose to report the frequency of mutations having fitness effects that met the *P*-value criteria in both replica experiments to limit the occurrence of false positives.

Mutant construction.

We constructed a total of 34 mutants across the three genes consisting of 12 *CAT-I* mutants, 13 *NDM-1* mutants, and 9 *aadB* mutants. We used inverse PCR to introduce the mutations. We also used inverse PCR to construct a control plasmid, pSKunk1-ΔGene, which had the coding region of the studied antibiotic resistance genes deleted.

For the C26D and C26S mutants in *NDM-1*, we found that an IS4-like element ISVsa5 family transposase insertion would occur within the *NDM-1* gene during the six hours of induced monoculture growth (Supplementary Text). We made two synonymous mutations within the 5'-GCTGAGC-3' insertion site that fully overlapped codons 23 and 24 to reduce transposase insertion and get an accurate measure of the collateral fitness effects for the C26D and C26S mutations. The new sequence was 5'-GTTATCA-3'. Inverse PCR was used to introduce these synonymous mutations. All mutant plasmids were transformed into NEB 5-alpha LacI^q electrocompetent cells.

Monoculture growth assay for fitness.

Cultures were grown following the same protocol described by Mehlhoff *et al*. (Mehlhoff et al. 2020). Briefly, we tracked the optical density of monocultures over six hours of induced growth with a dilution after three hours. We calculated the fitness using Equation 4 from the dilution factor (d) and the starting and final OD's (O_o, O_f) of the mutant and wild-type cultures under the assumption that the correlation between OD and cell density was the same for cells whether they were expressing wild-type or any mutant TEM-1 allele. Thus, fitness represents the mean growth rate of the cells expressing the mutant protein relative to the growth rate of cells expressing the wildtype protein.

$$w_i = \frac{\mu_i}{\mu_{wt}} = \frac{\left(\ln\frac{O_f d}{O_o}\right)_i}{\left(\ln\frac{O_f d}{O_o}\right)_{wt}} \quad (4)$$

Cell fractionation and analysis by PAGE and Western blot.

Cell cultures were grown as in the monoculture growth assay for fitness and then fractionated following a previously described procedure (Mehlhoff et al. 2020) based on the BugBuster reagent protocol for cell fractionation. Further description of measurement of the resulting protein concentration by DC Assay Kit (Bio-Rad) and sample preparation for SDS-PAGE can be found there as well. We loaded 15 µg of protein from fractionated samples in each lane for SDS-PAGE gels. Protein fractions were analyzed on 12% NuPAGE Bis-Tris gels (Thermo Fisher) in

MOPS running buffer. Gels were stained using Coomassie Brilliant Blue R-250 (Bio-Rad) to verify even loading of lanes. We performed immunoblots using rabbit Anti-CAT-I antibody (C9336; Sigma), rabbit Anti-NDM-1 antibody (MBS715336; MyBioSource), and rabbit Anti-AadB antibody (Cusabio custom antibody).

Since CAT-I is a homotrimer in its native form (Biswas et al. 2012), we used Native-PAGE and Western blots to see if the quaternary structure of CAT-I was affected by select mutations found to have deleterious collateral fitness effects. Samples for Native-PAGE were prepared using 15 µg of protein, 4X NativePAGE sample buffer (Invitrogen), 0.25 µl NativePAGE 5% G-250 Sample Additive, and nuclease-free water before being loaded onto a NativePAGE 4-16% Bis-Tris Gel (Thermo Fisher). The inner chamber of the electrophoresis system was filled with 1X NativePAGE Dark Blue Cathode Buffer (Thermo Fisher) while the outer chamber was filled with 1X NativePAGE Anode Buffer (Thermo Fisher). The gel was run for approximately two hours at 150 V with the 1X NativePAGE Dark Blue Cathode Buffer being replaced with 1X NativePAGE Light Blue Cathode Buffer (Thermo Fisher) after the dye front had migrated one third of the way through the gel. We then proceeded with Western blots as described.

Timescale of transposase insertion in C26D and C26S of NDM-1.
Monocultures of cells expressing C26D, C26S, and wild-type NDM-1 were grown to an OD of 0.5 before induction following the protocol for monoculture growth assays. We then diluted to an approximate OD of 0.2 and added 1 mM IPTG to each flask. Monocultures were grown for 6 hours with 10 ml of culture collected every hour for plasmid extraction. We diluted cultures back to an OD of 0.2 each hour to maintain exponential growth phase while still having enough cells available at the next hour for plasmid extraction. The resulting DNA was submitted for Sanger sequencing and run on a 1% agarose gel containing ethidium bromide for imaging under UV light.

Minimum inhibitory concentration (MIC) assays.
Cultures were grown overnight at 37°C in LB media containing 2% w/v glucose, 50 µg/ml spectinomycin, and 1 mM IPTG. The overnight cultures were then diluted to an OD of $1x10^{-5}$ before 50 µl of diluted culture was added to a plate and spread with an L-shaped spreader. Plates were made with 20 ml of LB-agar containing 2% w/v glucose, 50 µg/ml spectinomycin, and 1 mM IPTG. Differing levels of antibiotic were added to each plate depending on the MIC for the wild-type protein. For CAT-I, plates were made with 0, 16, 32, 64, 128, 256, 512, and 1024 µg/ml chloramphenicol. For NDM-1, plates were made with 0, 32, 64, 128, 256, 512, 1024, 2048, and 4096 µg/ml ampicillin. For AadB, plates were made with 0, 8, 16, 32, 64, 128, 256, and 512 µg/ml kanamycin. Plates were incubated for 16 hours at 37°C before colonies were counted. We identified the MIC as the antibiotic concentration at which there were fewer than 5% of the colony forming units (CFU) relative to a plate without antibiotics.

RNA-Seq Sample Preparation and Analysis.
Monocultures expressing the wildtype and all mutants for a given antibiotic resistance gene were grown on the same day along with an uninduced wild-type control. Samples for RNA-seq were prepared as described previously (Mehlhoff et al. 2020). The resulting double-stranded cDNA was pooled and submitted for Illumina TruSeq (2 x 75 bp) at the Single Cell and Transcriptomics Core facility at Johns Hopkins University.

Reads were inspected with FastQC (Andrews et al. 2018) to check per base sequence quality. We indexed the NEB 5-alpha F'Iq genome (NCBI Reference Sequence: NZ_CP053607.1) after having removed genes that appeared in both the episome and chromosomal DNA. Such genes had their counts otherwise overwritten as verified by mapping

to the NEB 5-alpha genome (NCBI Reference Sequence: NZ_CP017100.1). We mapped our paired end reads to the indexed NEB 5-alpha F'Iq transcriptome using STAR (Dobin et al. 2013). featureCounts (Liao et al. 2014) was used to quantify and tabulate transcript abundance while edgeR (Robinson et al. 2009) was used to tabulate the normalized counts per million.

RNA-Seq data analysis. Using Equation 5, we calculated a fold-difference in gene expression (g_i) from the counts of an individual gene from sample *i* (c_i), the counts of that same gene in the corresponding induced wild-type sample (c_{wt}), and total sequencing counts (c_T).

$$g_i = \frac{c_i c_{T,wt}}{c_{wt} c_{T,i}} \approx \frac{(c_i+0.5)c_{T,wt}}{(c_{wt}+0.5)c_{T,i}} \quad (5)$$

The variance in the fold-difference is then calculated from counts and the fold-difference in gene expression using Equation 6.

$$\sigma_{g_i}{}^2 = g_i{}^2 \left(\frac{1}{c_{wt}+0.5} - \frac{1}{c_{wt,T}} + \frac{1}{c_i+0.5} - \frac{1}{c_{i,T}}\right) \quad (6)$$

A 99% confidence interval, *Z*-score, and *P*-value were calculated following the method used in our deep sequencing analysis. Full equations are included in Mehlhoff *et al*. (Mehlhoff et al. 2020).

We primarily identified genes and more broadly, gene clusters and associated pathways, from the set of values in which there was a >2-fold difference in gene expression with $P<0.001$ significance. We utilized EcoCyc (Keseler et al. 2017) to further identify interconnected genes and search for patterns across genes which potentially play a role in deleterious collateral fitness effects.

PCR amplification of *traJ* and *traI* genes.
We grew monocultures of uninduced and induced wild-type CAT-I along with induced monocultures of the S27M and Q30M mutants following the monoculture growth assay outlined previously. We utilized the Qiagen Large-Construct Kit following the protocol for high yields of large-construct DNA without removal of genomic DNA. The *traJ* and *traI* genes were PCR amplified using 2X GoTaq Green MasterMix starting from 10 ng of template from each sample. PCR products were loaded on a 1% TAE gel containing ethidium bromide. Bands were visualized under UV light and imaged with Carestream Gel Logic 112.

Acknowledgements

This research was supported by National Science Foundation grants MCB-1817646 and MCB-2113019 to M.O.

Data availability

DMS sequencing data for *CAT-I*, *NDM-1*, and *aadB* can be found at BioProject (https://www.ncbi.nlm.nih.gov/bioproject) using accession no. PRJNA818255. RNA-Seq data are available at Gene Expression Omnibus at NCBI (https://www.ncbi.nlm.nih.gov/geo/) using accession no. GSE199248. Sequencing counts for the DMS studies can be found in **supplementary data S1-3**, Supplementary Material online. Sequencing counts for the RNA-Seq experiment can be found in **supplementary data S4**, Supplementary Material online.

References

Agozzino L, Dill KA. 2018. Protein evolution speed depends on its stability and abundance and on chaperone concentrations. *Proc. Natl. Acad. Sci. U. S. A.* 115:9092–9097.

Alvarez-Ponce D, Aguilar-Rodríguez J, Fares MA, Papp B. 2019. Molecular Chaperones Accelerate the Evolution of Their Protein Clients in Yeast. *Genome Biol. Evol.* 11:2360–2375.

Andrews S, Wingett SW, Hamilton RS. 2018. FastQ Screen : A tool for multi-genome mapping and quality control [version 2 ; referees : 4 approved] Referee Status : :1–13.

Auclair SM, Bhanu MK, Kendall DA. 2012. Signal peptidase I: Cleaving the way to mature proteins. *Protein Sci.* 21:13–25.

Awad A, Arafat N, Elhadidy M. 2016. Genetic elements associated with antimicrobial resistance among avian pathogenic Escherichia coli. *Ann. Clin. Microbiol. Antimicrob.* 15:1–8.

Bahr G, Vitor-Horen L, Bethel CR, Bonomo RA, Gonzalez LJ, Vila AJ. 2018. Clinical Evolution of New Delhi Metallo-β-Lactamase (NDM) optimizes resistance under Zn(II) Deprivation. *Antimicrob. Agents Chemother.* 62.

De Biase D, Tramonti A, Bossa F, Visca P. 1999. The response to stationary-phase stress conditions in Escherichia coli : role and regulation of the glutamic acid decarboxylase system. *Mol. Microbiol.* 32:1198–1211.

Biesiadecka MK, Sliwa P, Tomala K, Korona R. 2020. An Overexpression Experiment Does Not Support the Hypothesis That Avoidance of Toxicity Determines the Rate of Protein Evolution. *Genome Biol. Evol.* 12:589–596.

Biswas T, Houghton JL, Garneau-Tsodikova S, Tsodikov O V. 2012. The structural basis for substrate versatility of chloramphenicol acetyltransferase CAT I. *Protein Sci.* 21:520–530.

Bolger AM, Lohse M, Usadel B. 2014. Trimmomatic : a flexible trimmer for Illumina sequence data. 30:2114–2120.

Bosley AD, Ostermeier M. 2005. Mathematical expressions useful in the construction , description and evaluation of protein libraries. 22:57–61.

Bratulic S, Gerber F, Wagner A. 2015. Mistranslation drives the evolution of robustness in TEM-1 β-lactamase. *Proc. Natl. Acad. Sci. U. S. A.* 112:12758–12763.

Cheng Z, Thomas PW, Ju L, Bergstrom A, Mason K, Clayton D, Miller C, Bethel CR, VanPelt J, Tierney DL, et al. 2018. Evolution of New Delhi metallo-β-lactamase (NDM) in the clinic: Effects of NDM mutations on stability, zinc affinity, and mono-zinc activity. *J. Biol. Chem.* 293:12606–12618.

Cox G, Stogios PJ, Savchenko A, Wright GD. 2015. Structural and molecular basis for resistance to aminoglycoside antibiotics by the adenylyltransferase ANT(2″)-Ia. *MBio* 6:1–9.

Dobin A, Davis CA, Schlesinger F, Drenkow J, Zaleski C, Jha S, Batut P, Chaisson M, Gingeras TR. 2013. STAR - ultrafast universal RNA-seq aligner. 29:15–21.

Firnberg E, Ostermeier M. 2012. PFunkel: Efficient, Expansive, User-Defined Mutagenesis. *PLoS One* 7:1–10.

Flores-Kim J, Darwin AJ. 2016. The Phage Shock Protein Response. *Annu. Rev. Microbiol.* 70:83–101.

Geiler-Samerotte KA, Dion MF, Budnik BA, Wang SM, Hartl DL, Drummond DA. 2011. Misfolded proteins impose a dosage-dependent fitness cost and trigger a cytosolic unfolded protein response in yeast. *Proc. Natl. Acad. Sci. U. S. A.* 108:680–685.

González LJ, Bahr G, Nakashige TG, Nolan EM, Bonomo RA, Vila AJ. 2016. Membrane anchoring stabilizes and favors secretion of New Delhi metallo-β-lactamase. *Nat. Chem. Biol.* 12:516–522.

Goodale A, Michailidis F, Watts R, Chok SC, Hayes F. 2020. Characterization of permissive and non-permissive peptide insertion sites in chloramphenicol acetyltransferase. *Microb.*

Pathog.:104395.
Grabowicz M, Silhavy TJ. 2017. Envelope Stress Responses: An Interconnected Safety Net. *Trends Biochem. Sci.* 42:232–242.
Guo Y, Wang J, Niu G, Shui W, Sun Y, Zhou H, Zhang Y, Yang C, Lou Z, Rao Z. 2011. A structural view of the antibiotic degradation enzyme NDM-1 from a superbug. *Protein Cell* 2:384–394.
Halling SM, Kleckner N. 1982. A symmetrical six-base-pair target site sequence determines Tn10 insertion specificity. *Cell* 28:155–163.
Holden ER, Webber MA. 2020. MarA, RamA, and SoxS as Mediators of the Stress Response: Survival at a Cost. *Front. Microbiol.* 11:1–10.
Jahn TR, Radford SE. 2008. Folding versus aggregation: polypeptide conformations on competing pathways. *Arch. Biochem. Biophys.* 469:100–117.
Kaminska R, Van Der Woude MW. 2010. Establishing and maintaining sequestration of dam target sites for phase variation of agn43 in Escherichia coli. *J. Bacteriol.* 192:1937–1945.
Keseler IM, Mackie A, Santos-Zavaleta A, Billington R, Bonavides-Martínez C, Caspi R, Fulcher C, Gama-Castro S, Kothari A, Krummenacker M, et al. 2017. The EcoCyc database: Reflecting new knowledge about Escherichia coli K-12. *Nucleic Acids Res.* 45:D543–D550.
King D, Strynadka N. 2011. Crystal structure of New Delhi metallo-β-lactamase reveals molecular basis for antibiotic resistance. *Protein Sci.* 20:1484–1491.
Krylov DM, Wolf YI, Rogozin IB, Koonin E V. 2003. Gene loss, protein sequence divergence, gene dispensability, expression level, and interactivity are correlated in eukaryotic evolution. *Genome Res.* 13:2229–2235.
Laganenka L, Colin R, Sourjik V. 2016. Chemotaxis towards autoinducer 2 mediates autoaggregation in Escherichia coli. *Nat. Commun.* 7:1–10.
Lemos B, Bettencourt BR, Meiklejohn CD, Hartl DL. 2005. Evolution of proteins and gene expression levels are coupled in Drosophila and are independently associated with mRNA abundance, protein length, and number of protein-protein interactions. *Mol. Biol. Evol.* 22:1345–1354.
Levy ED, De S, Teichmann SA. 2012. Cellular crowding imposes global constraints on the chemistry and evolution of proteomes. *Proc. Natl. Acad. Sci. U. S. A.* 109:20461–20466.
Liao Y, Smyth GK, Shi W. 2014. FeatureCounts: An efficient general purpose program for assigning sequence reads to genomic features. *Bioinformatics* 30:923–930.
Mehlhoff JD, Ostermeier M. 2020. Biological fitness landscapes by deep mutational scanning. 1st ed. Elsevier Inc. Available from: http://dx.doi.org/10.1016/bs.mie.2020.04.023
Mehlhoff JD, Stearns FW, Rohm D, Wang B, Tsou E, Dutta N, Hsiao M-H, Gonzalez CE, Rubin AF, Ostermeier M. 2020. Collateral fitness effects of mutations. *Proc. Natl. Acad. Sci.* 117:11597–11607.
Mironov A, Seregina T, Shatalin K, Nagornykh M, Shakulov R, Nudler E. 2020. CydDC functions as a cytoplasmic cystine reductase to sensitize Escherichia coli to oxidative stress and aminoglycosides. *Proc. Natl. Acad. Sci. U. S. A.* 117:23565–53570.
Navarro S, Villar-Piqué A, Ventura S. 2014. Selection against toxic aggregation-prone protein sequences in bacteria. *Biochim. Biophys. Acta - Mol. Cell Res.* 1843:866–874.
Olzscha H, Schermann SM, Woerner AC, Pinkert S, Hecht MH, Tartaglia GG, Vendruscolo M, Hayer-Hartl M, Hartl FU, Vabulas RM. 2011. Amyloid-like aggregates sequester numerous metastable proteins with essential cellular functions. *Cell* 144:67–78.
Parsell DA, Sauer RT. 1989. Induction of a heat shock-like response by unfolded protein in Escherichia coli: dependence on protein level not protein degradation. *Genes Dev.* 3:1226–1232.
Peralta DR, Adler C, Corbalán NS, Paz García EC, Pomares MF, Vincent PA. 2016. Enterobactin as part of the oxidative stress response repertoire. *PLoS One* 11:1–15.

Prunotto A, Bahr G, González LJ, Vila AJ, Peraro MD. 2020. Molecular Bases of the Membrane Association Mechanism Potentiating Antibiotic Resistance by New Delhi Metallo-β-Lactamase 1. *ACS Infect Dis.* 6:2719-2731.
Raivio TL. 2014. Everything old is new again: An update on current research on the Cpx envelope stress response. *Biochim. Biophys. Acta - Mol. Cell Res.* 1843:1529–1541.
Reis AC, Salis HM. 2020. An automated model test system for systematic development and improvement of gene expression models. *ACS Synth. Biol.* 9:3145–3156.
Robinson MD, McCarthy DJ, Smyth GK. 2009. edgeR: A Bioconductor package for differential expression analysis of digital gene expression data. *Bioinformatics* 26:139–140.
Rubin AF, Gelman H, Lucas N, Bajjalieh SM, Papenfuss AT, Speed TP, Fowler DM. 2017. A statistical framework for analyzing deep mutational scanning data. 1–15.
Van der Schueren J, Robben J, Goossens K, Heremans K, Volckaert G. 1996. Identification of Local Carboxy-terminal Hydrophobic Interactions Essential for Folding or Stability of Chloramphenicol Acetyltransferase. *J. Mol. Biol.* 256:878–888.
Sohka T, Heins RA, Phelan RM, Greisler JM, Townsend CA, Ostermeier M. 2009. An externally tunable bacterial band-pass filter. *Proc. Natl. Acad. Sci.* 106:10135–10140.
Stamatakis A, Zhang J, Kobert K. 2014. PEAR : a fast and accurate Illumina Paired-End reAd mergeR. 30:614–620.
Storey JD, Tibshirani R. 2003. Statistical significance for genomewide studies. *Proc. Natl. Acad. Sci.* 100:9440-9445.
Sun Z, Hu L, Sankaran B, Prasad BVV, Palzkill T. 2018. Differential active site requirements for NDM-1 β-lactamase hydrolysis of carbapenem versus penicillin and cephalosporin antibiotics. *Nat. Commun.* 9.
Taverna DM, Goldstein RA. 2002. Why are proteins marginally stable? *Proteins* 46:105–109.
Thomas PW, Zheng M, Wu S, Guo H, Liu D, Xu D, Fast W. 2011. Characterization of purified New Delhi metallo-β-lactamase-1. *Biochemistry* 50:10102–10113.
Tucker DL, Foster JW, Miranda RL, Cohen PS, Conway T. 2003. Genes of the GadX-GadW Regulon in. *Society* 185:3190–3201.
Usmanova DR, Plata G, Vitkup D. 2021. The Relationship between the Misfolding Avoidance Hypothesis and Protein Evolutionary Rates in the Light of Empirical Evidence. *Genome Biol. Evol.* 13.
Wall E, Majdalani N, Gottesman S. 2018. The Complex Rcs Regulatory Cascade. *Annu. Rev. Microbiol.* 72:111-139.
Wright E, Serpersu EH. 2005. Enzyme-substrate interactions with an antibiotic resistance enzyme: Aminoglycoside nucleotidyltransferase(2″)-Ia characterized by kinetic and thermodynamic methods. *Biochemistry* 44:11581–11591.
Wu Z, Cai X, Zhang X, Liu Y, Tian G-B, Yang J-R, Chen X. 2022. Expression level is a major modifier of the fitness landscape of a protein coding gene. *Nat. Ecol. Evol.* 6:103–115.
Yang JR, Liao BY, Zhuang SM, Zhang J. 2012. Protein misinteraction avoidance causes highly expressed proteins to evolve slowly. *Proc. Natl. Acad. Sci. U. S. A.* 109:831–840.
Yong D, Toleman MA, Giske CG, Cho HS, Sundman K, Lee K, Walsh TR. 2009. Characterization of a new metallo-β-lactamase gene, bla NDM-1, and a novel erythromycin esterase gene carried on a unique genetic structure in Klebsiella pneumoniae sequence type 14 from India. *Antimicrob. Agents Chemother.* 53:5046–5054.
Zalucki YM, Jen FEC, Pegg CL, Nouwens AS, Schulz BL, Jennings MP. 2020. Evolution for improved secretion and fitness may be the selective pressures leading to the emergence of two NDM alleles. *Biochem. Biophys. Res. Commun.* 524:555–560.
Zhang J, Yang JR. 2015. Determinants of the rate of protein sequence evolution. *Nat. Rev. Genet.* 16:409–420.

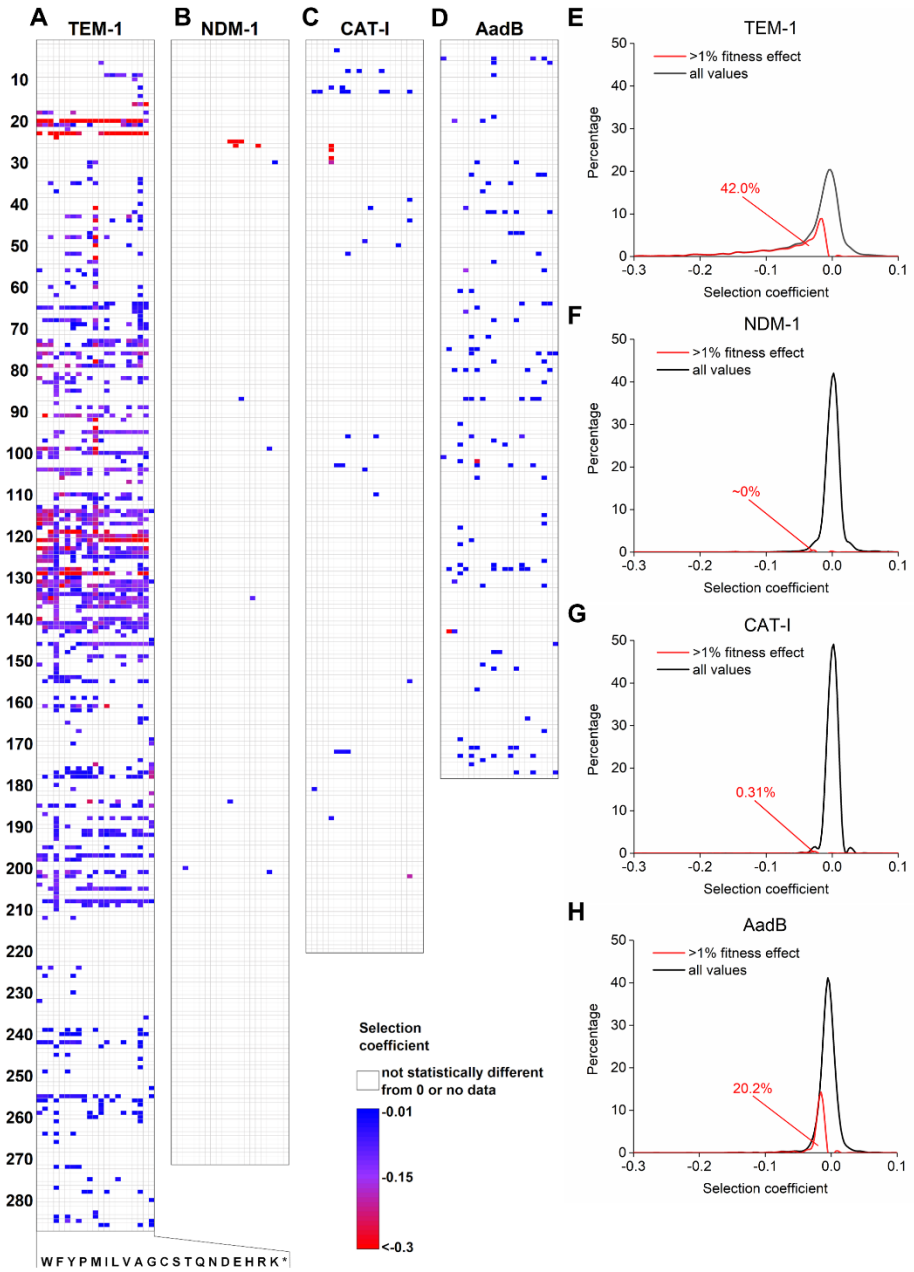

Fig. 1. Deleterious collateral fitness effects of nonsynonymous mutations in TEM-1, NDM-1, CAT-I, and AadB. Heat map of weighted mean selection coefficients for mutations that caused significant deleterious collateral fitness effects (*P*<0.01) in both replica experiments in (**A**) TEM-1, (**B**) NDM-1, (**C**) CAT-I, and (**D**) AadB. . Detailed heat maps showing all fitness values are available as **supplementary figs. 6,7,8**, Supplementary Material online. DFE showing collateral fitness effects for missense substitutions in (**E**) TEM-1, (**F**) NDM-1, (**G**) CAT-I, and (**H**) AadB. The red curve and percentage indicate the estimated portion of missense mutations that cause a greater than 1% decrease in fitness by analyzing the symmetry of the distribution about the value of zero.

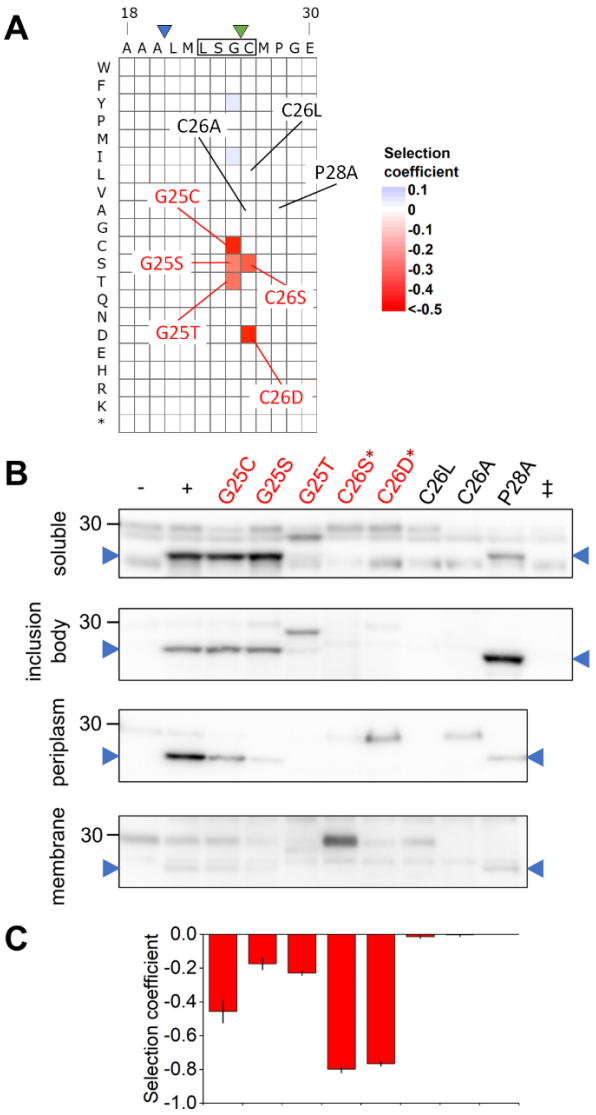

Fig. 2. NDM-1 mutations' effect on fitness and protein fate. (**A**) Subsection of the NDM-1 collateral fitness landscape showing weighted mean selection coefficients (by DMS) for selected mutations (P<0.01 in both replicates). The LSGC lipobox is indicated with a rectangle. Expected NDM-1 signal sequence cleavage sites include a signal peptidase I site (blue triangle) and signal peptidase II site (green triangle). (**B**) Western blots of the total soluble, inclusion body, periplasmic, and membrane fractions from cells expressing unmutated NDM-1 (–, without IPTG; +, with IPTG) or the indicated NDM-1 mutants (deleterious mutations in red and neutral mutations in black). The C26S* and C26D* mutants include two synonymous mutations to prevent transposase insertion (SI Appendix, Supplementary Text). Samples from cells expressing CAT-I (‡) were included to identify the bands of cross-reacting *E. coli* proteins. The blue arrowhead indicates the expected position of mature NDM-1. Full western blots including the second biological replicate are provided as **supplementary fig. S9**, Supplementary Material online. (**C**) Selection coefficients were determined from monoculture growth experiments by measuring the mean growth rate over six hours of growth post-induction. Error bars represent 99% confidence intervals (n=3).

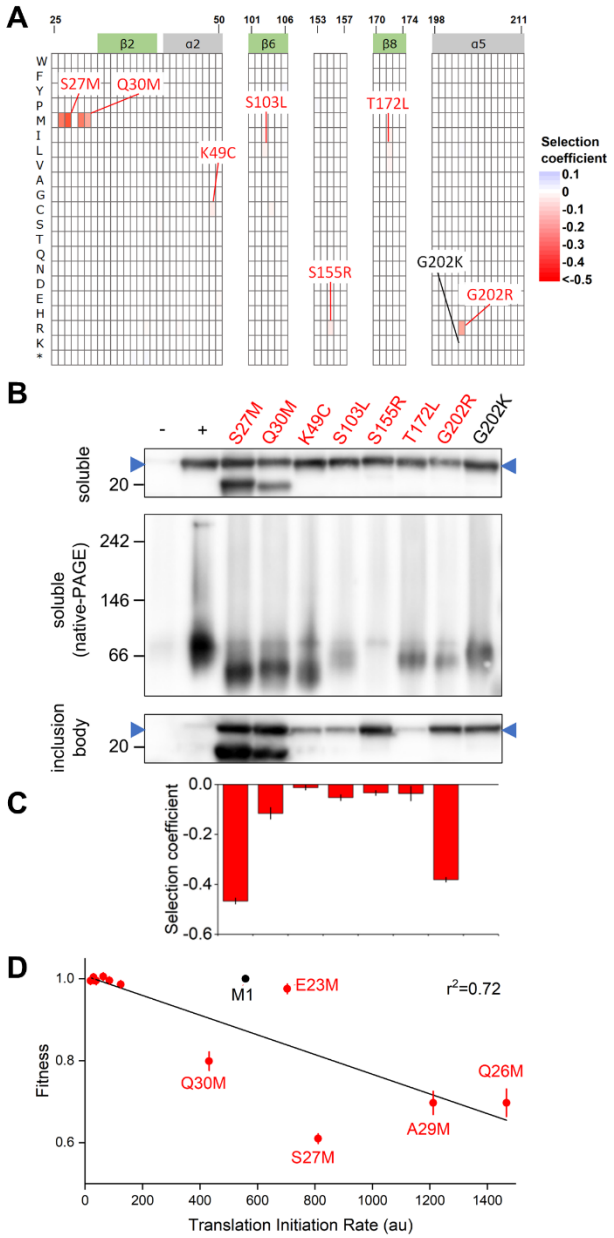

Fig. 3. CAT-I mutations' effect on fitness and protein fate. (**A**) Subsections of the CAT-I collateral fitness landscape showing weighted mean selection coefficients (by DMS) for selected mutations (*P*<0.01 in both replicates). Regions containing β-sheets (green) and α-helices (grey) are labeled along the top. (**B**) Western blots of the total soluble (denaturing and native gels) and inclusion body fractions from cells expressing unmutated CAT-I (–, without IPTG; +, with IPTG) or the indicated CAT-I mutants (deleterious mutations in red and neutral mutations in black). The blue arrowhead indicates the expected position of CAT-I. Full western blots including the second biological replicate are provided as **supplementary fig. S11**, Supplementary Material online. (**C**) Selection coefficients were determined from monoculture growth experiments by measuring the mean growth rate over six hours of growth post-induction. Error bars represent 99% confidence intervals (*n*=3). (**D**) Experimental weighted mean fitness values plotted as a function of predicted translation initiation rates at residues 22-34 when the position is mutated to

methionine. M1 represents the wild-type start codon and is excluded from the fit. A table of the predicted translation initiation rates and corresponding collateral fitness values for these mutations is included as **supplementary table S1**, Supplementary Material online.

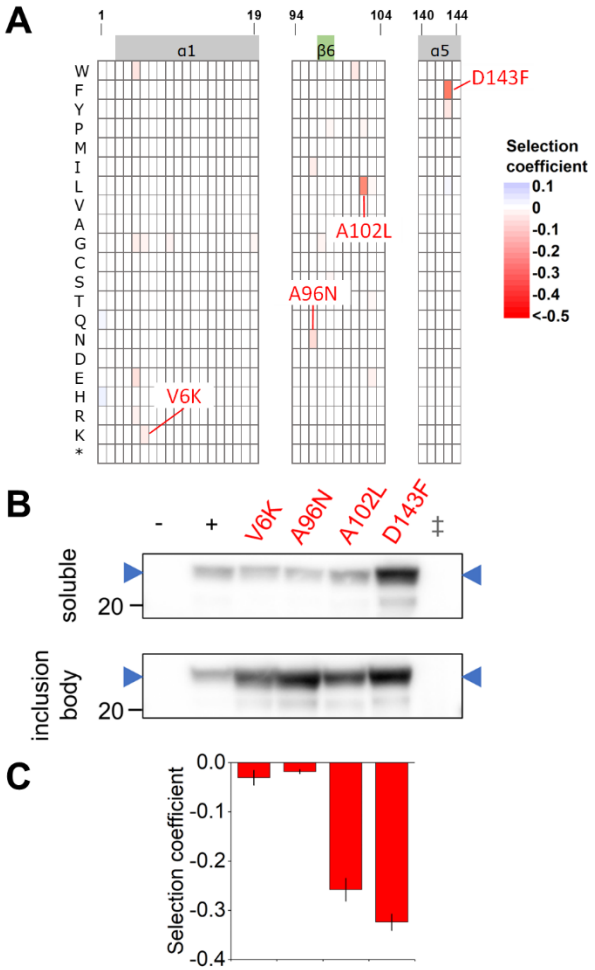

Fig. 4. AadB mutations' effect on fitness and protein fate. (**A**) Subsection of the AadB collateral fitness landscape showing weighted mean selection coefficients (by DMS) for selected mutations (P<0.01 in both replicates). Regions containing β-sheets (green) and α-helices (grey) are labeled along the top. (**B**) Western blots of the total soluble and inclusion body fractions from cells expressing unmutated AadB (–, without IPTG; +, with IPTG) or the indicated AadB mutants (deleterious mutations in red and neutral mutations in black). Samples from cells expressing CAT-I (‡) were included to identify the bands of cross-reacting *E. coli* proteins. The blue arrowhead indicates the expected position of AadB. Full western blots including the second biological replicate are provided as **supplementary fig. S12**, Supplementary Material online. (**C**) Selection coefficients were determined from monoculture growth experiments by measuring the mean growth rate over six hours of growth post-induction. Error bars represent 99% confidence intervals (n=3).

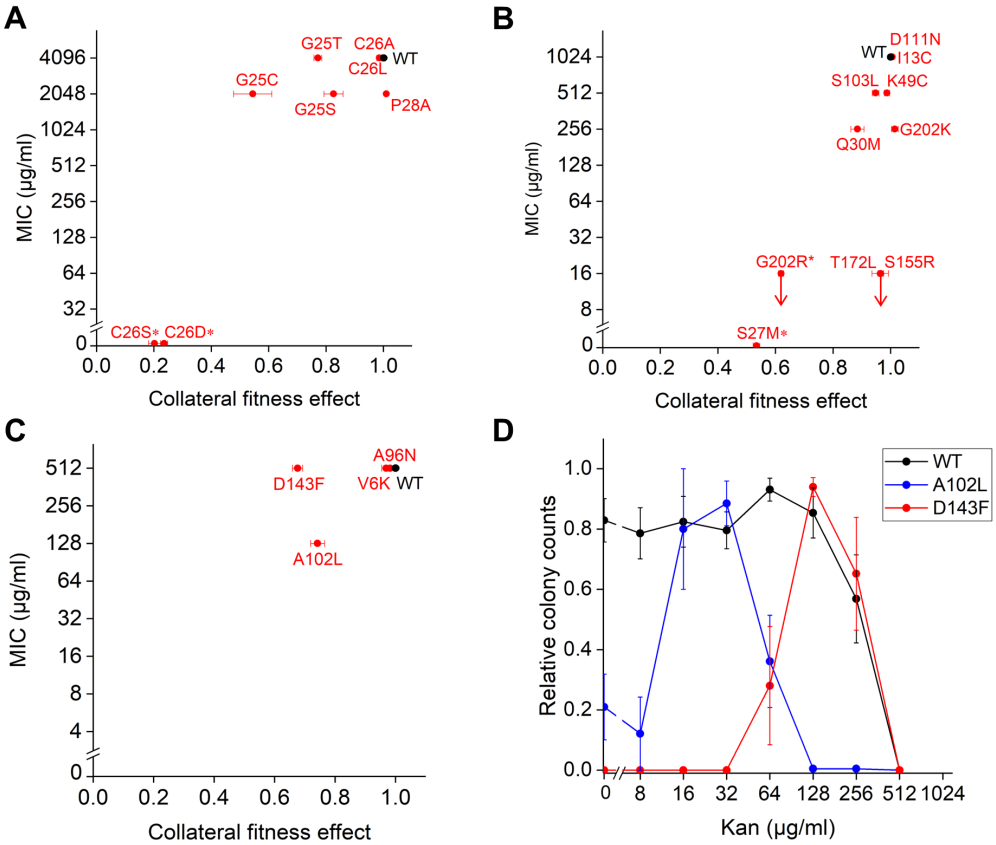

Fig. 5. Comparison of primary and collateral fitness effects. We utilized a minimum inhibitory concentration (MIC) assay in which cells expressing wild-type or mutants of the antibiotic resistance genes were grown overnight with IPTG inducer and plated on agar plates containing the corresponding antibiotic. Plots showing the median MIC values for cells expressing (**A**) *NDM-1* variants plated on ampicillin-containing plates, (**B**) *CAT-I* variants plated on chloramphenicol-containing plates, and (**C**) *aadB* variants plated on kanamycin-containing plates as a function of collateral fitness effects as measured by monoculture growth. Error bars represent the 99% confidence interval. Red arrows indicate a MIC of <16 µg/ml for G202R, T172L, and S155R. Variants that did not form colonies on a plate lacking antibiotics in at least one replicate of the assay are marked with an (*). (**D**) Mean relative colony counts in the MIC assays for the wild-type *aadB* and A102L and D143F mutants. Error bars are standard error of the mean (n=5). Plots of mean relative colony counts for all MIC assay samples are included as **supplementary fig. S13**, Supplementary Material online. A complete table of MIC values is provided as **supplementary table S2**, Supplementary Material online with colony counts from the assay available as **supplementary data S5**, Supplementary Material online.

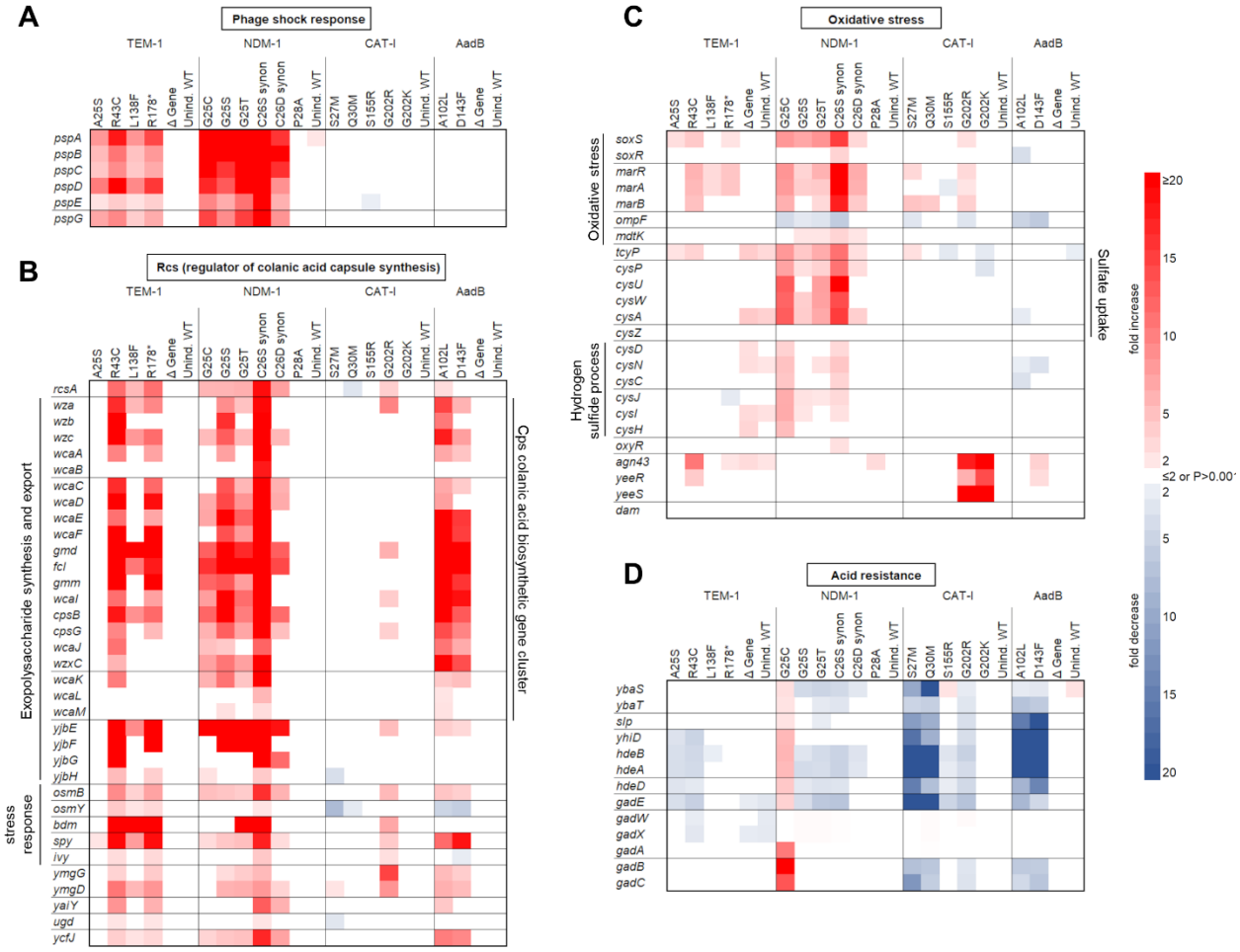

Fig. 6. Effects of mutations with deleterious collateral fitness effects on *E. coli* transcriptome. We collected exponentially growing cells after approximately 330 minutes of induced growth and performed RNA-Seq experiments to monitor expression levels of genes throughout the transcriptome. The heat maps show select genes in the (**A**) phage shock protein (Psp) response (**B**) regulator of colanic acid capsule synthesis (Rcs) pathway (**C**) oxidative stress responses, and the (**D**) GAD acid resistance response that differed by greater than twofold expression (P<0.001, Z-test) relative to cells expressing the wild-type antibiotic resistance genes. Control samples include ones in which wildtype gene expression was not induced (Unind. WT) and induced ones which lack the gene (Δ Gene). RNA-Seq data from representative mutations in *TEM-1* is from Mehlhoff *et al.* (Mehlhoff et al. 2020). Additional observations of gene expression are provided as **supplementary text** and **fig. S16**, Supplementary Material online. Tabulated RNA-Seq data is provided as **supplementary data S4**, Supplementary Material online.

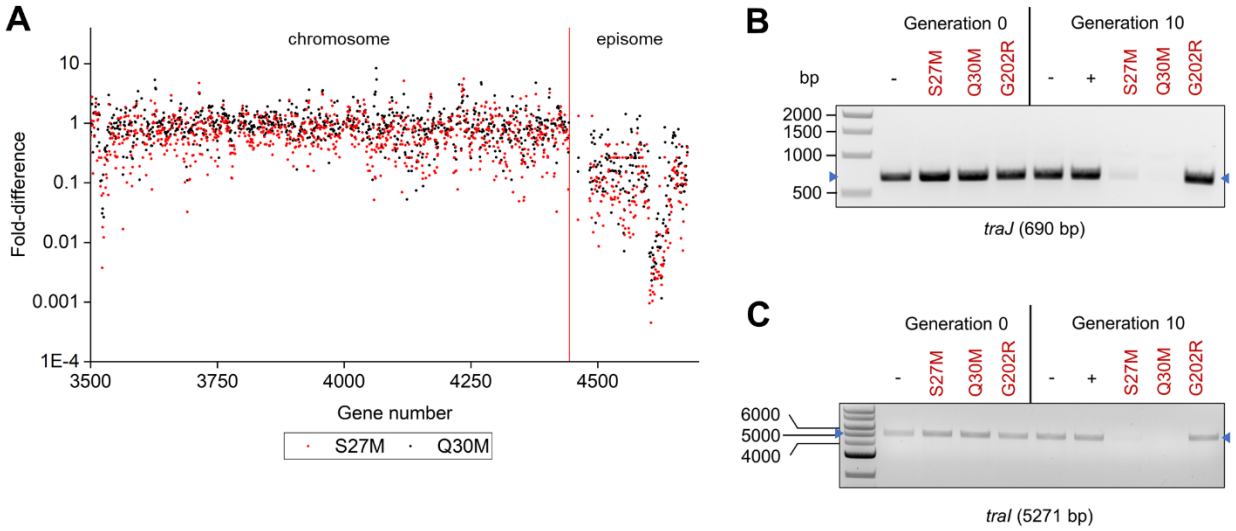

Fig. 7. Loss of episome corresponding to deleterious methionine substitutions in CAT-I. RNA-Seq revealed the S27M and Q30M methionine substitutions in *CAT-I* led to (**A**) reduced expression of episomal genes after 10 generations of induced growth. All genes to the right of the red line are on the episome. PCR amplification of the (**B**) *traJ* and (**C**) *traI* episomal genes illustrate the loss of these genes in cells expressing the S27M or Q30M mutants of CAT-I. The G202R CAT-I mutation represents a mutation causing large-magnitude deleterious effects (like S27M and Q30M) but no change in *traJ* and *traI* expression.

Supplementary Materials for

Genes vary greatly in their propensity for collateral fitness effects of mutations

Jacob D. Mehlhoff and Marc Ostermeier*

Department of Chemical and Biomolecular Engineering, Johns Hopkins University, 3400 N. Charles St., Baltimore, MD, 21218, USA

*Corresponding author: Email: oster@jhu.edu

This PDF file includes:

Supplementary Text
Figs. S1 to S17
Table S1 to S2
Supplementary References
Captions for Data S1 to S5

Other Supplementary Materials for this manuscript include the following:

Data S1 to S5

Supplementary Text

Artifactual fitness values at select residues in NDM-1 and AadB

From the DMS studies for *NDM-1*, we measured apparent beneficial fitness effects in both biological replicates at residues 26-28 (**supplementary fig. S3A-C**, Supplementary Material online). For residues 132-134 we observed widespread deleterious fitness effects in the first replicate, but widespread beneficial effects of approximately 4% in replica 2. For *aadB*, we measured widespread beneficial fitness effects of approximately 3-6% at residues 155 and 156 for both replicates of DMS (**supplementary fig. S4A,B**, Supplementary Material online). We believe these systematic beneficial fitness effects at these positions are artifactual and not true beneficial collateral fitness effects. Foremost in our reasoning, these beneficial fitness effects in *NDM-1* and *aadB* were not reproducible by monoculture growth experiments for the selected mutants that we tested (**supplementary fig. S5**, Supplementary Material online). Furthermore, these apparent fitness effects are near-universal in the DMS measurements across all substitutions at these positions including nonsense mutations. If nonsense mutations were in fact alleviating the effects of expressing a toxic protein, we would expect to see more widespread beneficial effects at nonsense mutations throughout the protein or beneficial effects from mutations at the start codon. We do not find evidence of either in the DMS data or growth studies with cells expressing *NDM-1* and *aadB*. In addition, the sequencing counts at these positions tend to have abnormally high counts and/or result in abnormally high standard deviations relative to the mean. This can be seen by plotting the ratio between the standard deviation of fitness effects at a position and the mean fitness at that position as a function of total counts. We expect the ratio to increase due to noise at low total count values. At high values of total counts, the ratio should go to a limiting, finite value. We find residues 26-28 and 132-134 in *NDM-1* to be outliers in this plot (**supplementary fig. S3D**, Supplementary Material online). Similarly, residue 156 stands out as an outlier in the plot for *aadB* (**supplementary fig. S4C**, Supplementary Material online). We speculate these artifacts stem from sequencing artifacts and/or with the creation of the amplicons by PCR, but we do not have a specific hypothesis. Because of our lack of confidence in these effects, we do not include them in our analysis. We removed the wild-type synonym counts for residues A155 and C156 of *aadB* region 2 and C26 and P28 of *NDM-1* region 1 so that they would not affect the fitness values calculated when using the wild-type synonym alleles as a reference.

Additional changes in gene expression.

We enumerate additional genes we identified whose expression was affected by mutations causing collateral fitness effects.

Expression of genes corresponding to biofilm formation increased for many of the deleterious NDM-1 mutations while genes corresponding to pilus formation, notably belonging to the *fim* and *ecp* operons, decreased in expression (**supplementary fig. S16A**, Supplementary Material online). We note the increase in expression for many of these genes alongside those belonging to the Rcs pathway as further evidence of the biofilm response seen in deleterious mutants.

In contrast, many of the cold-shock proteins are expressed at reduced levels in cells expressing deleterious mutations (**supplementary fig. S16B**, Supplementary Material online). Absence of proteins coded by the *cspIBF* operon results in a competitive disadvantage in stationary phase (Kram et al. 2020). We find that the cultures with higher ODs at the end of the growth period tend to have increased expression of these cold-shock proteins and believe they may be beginning to transition to stationary phase.

We also find increased expression of genes belonging to the fructose catabolic process within cells expressing deleterious mutations of *NDM-1*, *CAT-I*, and *aadB* (**supplementary fig.**

S16C, Supplementary Material online) although we do not have a proposed mechanism by which these mutations would lead to such increase in expression.

In our previous RNA-Seq experiments with TEM-1, we noted some samples displayed differential expression for genes regulated by FNR. The FNR-regulated operons include genes which are involved in anaerobic respiration (Partridge et al. 2007) along with the transition from aerobic to micro-anaerobic growth conditions in the presence of nitrate (Constantinidou et al. 2006). We find some of these same differential expression patterns in our RNA-seq experiments for the current study (**supplementary fig. S17**, Supplementary Material online). However, such effects are mainly limited to select samples from the CAT-I gene. We suspect the variability across samples pertains to the availability of oxygen during the processing steps between the end of the monoculture growth assay and RNA extraction. We did not find the differential expression for FNR-regulated operons to impact gene expression in the stress-response pathways.

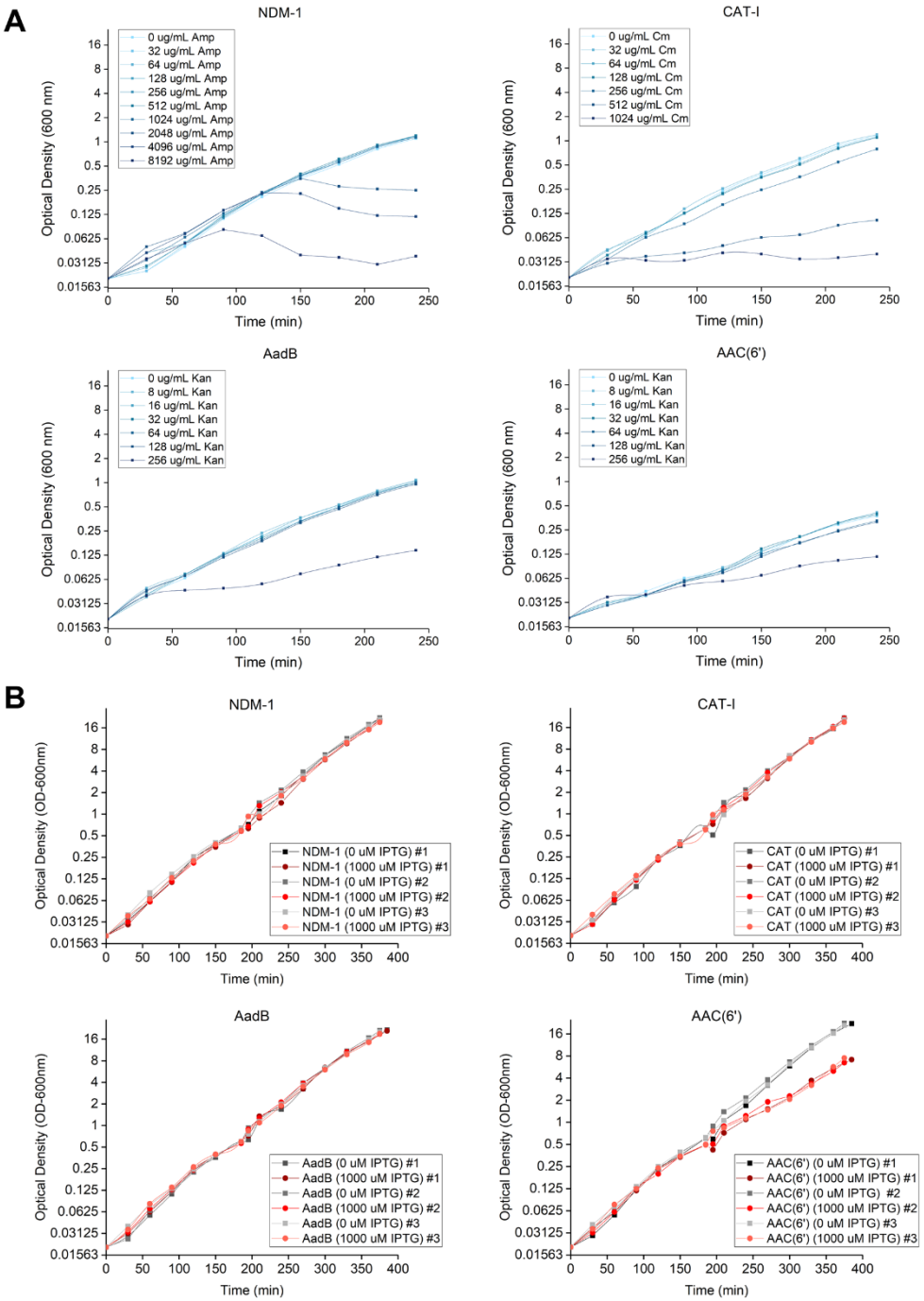

Figure S1. Effect of expressing antibiotic resistance genes. (**A**) Confirmation of conferral of antibiotic resistance. Antibiotics were added at the indicated concentrations to exponentially growing cells expressing the *NDM-1*, *CAT*-I, *aadB*, or *aac(6')-Im* antibiotic resistance genes in order to verify their ability to confer antibiotic resistance and assess the cells level of resistance. (**B**) Fitness effect of expression of the antibiotic resistance genes. At time zero, exponentially growing cultures were diluted in two shake flasks to an OD of 0.020 and final volume of 100 ml using LB media which had been prewarmed to 37°C. IPTG was introduced to one of the flasks at a concentration of 1 mM. No IPTG was added to the second flask. Both flasks were incubated at 37°C with shaking and optical density at 600 nm (OD-600 nm) was monitored every 30 minutes for six hours. After approximately three hours, the culture was diluted into fresh LB media (with or without IPTG as appropriate) to maintain growth in exponential phase. The OD

measurements after this dilution are relative values in which the measured OD value is multiplied by the dilution factor. From the OD at the start and end of growth and the number of generations, we calculated a fitness effect for expressing each of the antibiotic resistance genes. The average fitness effects of expression in three replica experiments were +1.06% ± 0.06%, -0.33 ± 0.56%, -0.95 ± 0.33%, and -16.14 ± 1.15% for *NDM-1*, *CAT-I*, *aadB*, and *aac(6')-Im*, respectively.

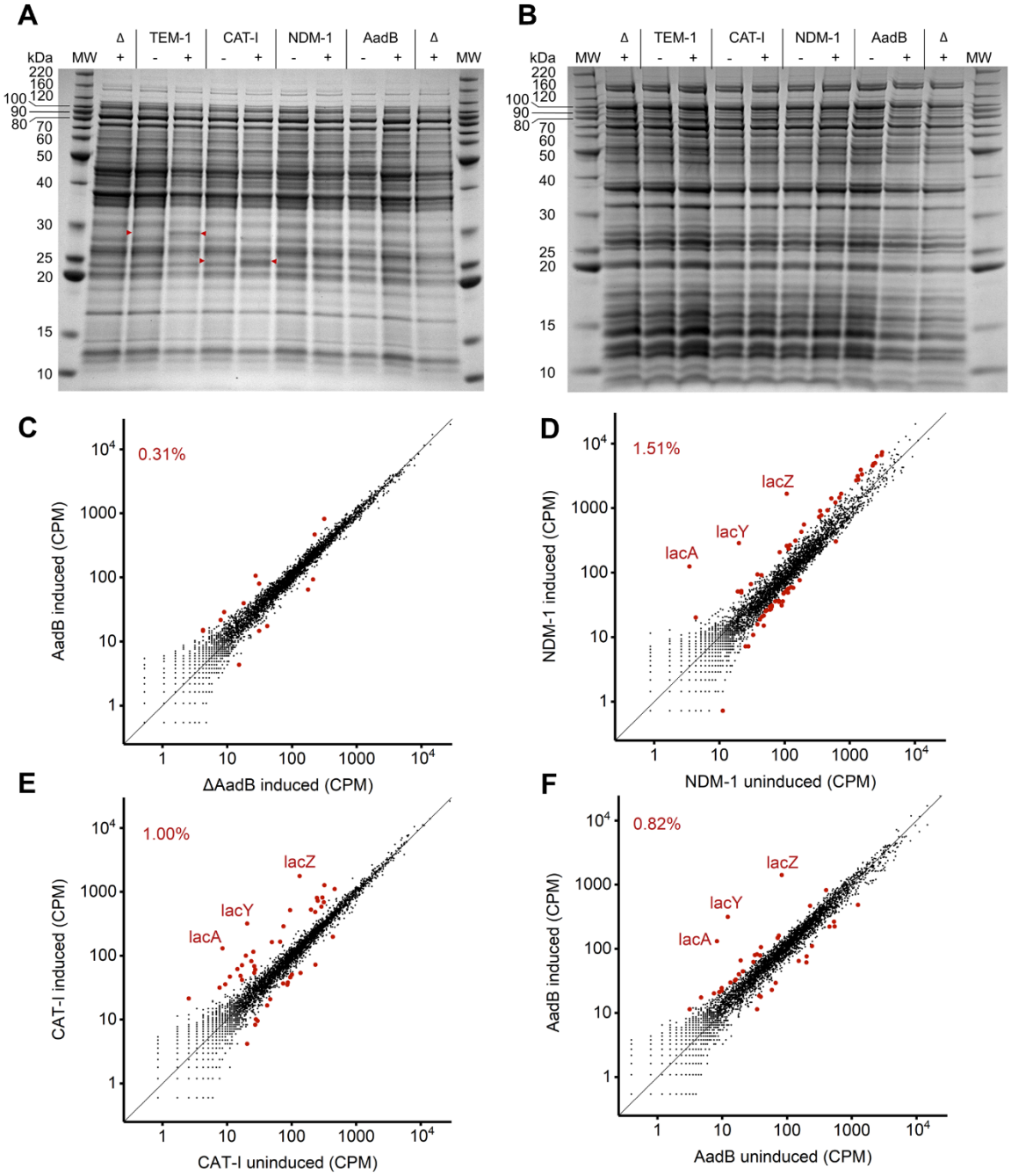

Figure S2. Expression of wild-type antibiotic resistance proteins and their effects. SDS-PAGE gel of cell extracts of (**A**) total soluble protein and (**B**) total insoluble protein from NEB 5-alpha F'lacI^q *E. coli* cells containing pSKunk-1-TEM-1, pSKunk-1-CAT-I, pSKunk-1-NDM-1, pSKunk-1-AadB, or the Δ gene control which has the antibiotic resistance gene deleted from the plasmid. Expression of the antibiotic resistance genes was controlled under the *tac* promoter and either uninduced (-) or induced (+) with 1 mM IPTG. Visible changes in expression of a protein band at the expected size of the expressed protein are marked with a red triangle. Bands for NDM-1 and AadB were not observed, but western blots confirmed expression. The expected sizes of the antibiotic resistance proteins are 28.9 kDa for mature TEM-1, 25.7 kDa for CAT-I, 25.9 kDa for mature NDM-1, and 19.9 kDa for AadB. (**C**) RNA-Seq results showing the effect of AadB expression on the *E. coli* transcriptome using Δ gene plasmid as the

comparison. RNA-Seq results comparing gene expression in *E. coli* cells expressing (**D**) NDM-1, (**E**) CAT-I, and (**F**) AadB relative to cultures lacking the IPTG inducer. IPTG induces expression of the *lacZYA* operon. Genes with at least a 2-fold change in expression at $P<0.001$ (Z-test) significance are indicated with a larger, red circle and the percentage of genes that meet these criteria is indicated on each plot. CPM = counts per million.

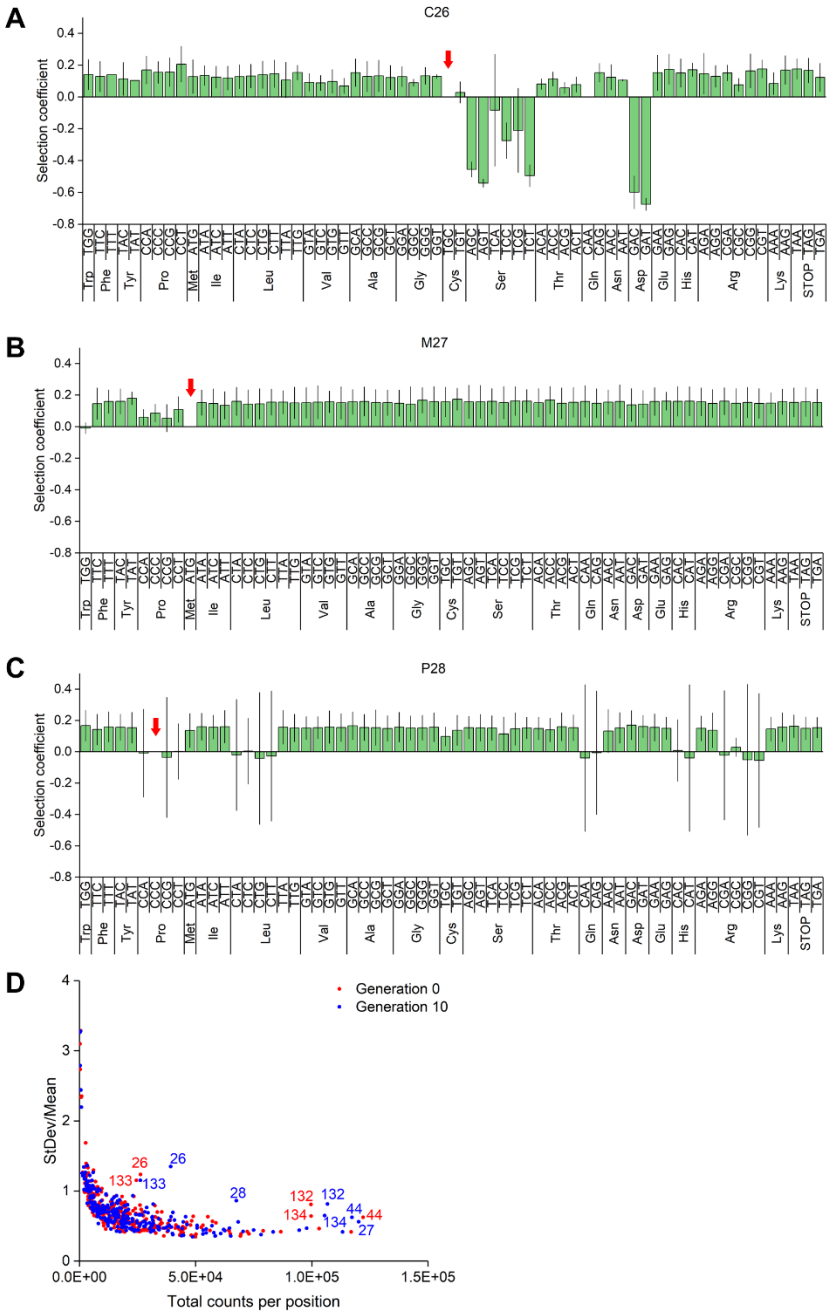

Figure S3. Artifactual beneficial fitness effects at residues 26-28 of NDM-1. Weighted mean collateral fitness effects of mutations in (**A**) C26, (**B**) M27, and (**C**) P28 as measured by two replica DMS growth competition experiments. Red arrow indicates wild-type codon. Error bars are 99% confidence intervals. (**D**) Plot of the standard deviation of all fitness measurements for nonsynonymous mutations at a specific residue divided by the mean fitness at that residue as a function of the total counts at the position. Data in red represents counts of a specific allele from before induction and data in blue represents counts of an allele after ten generations of growth.

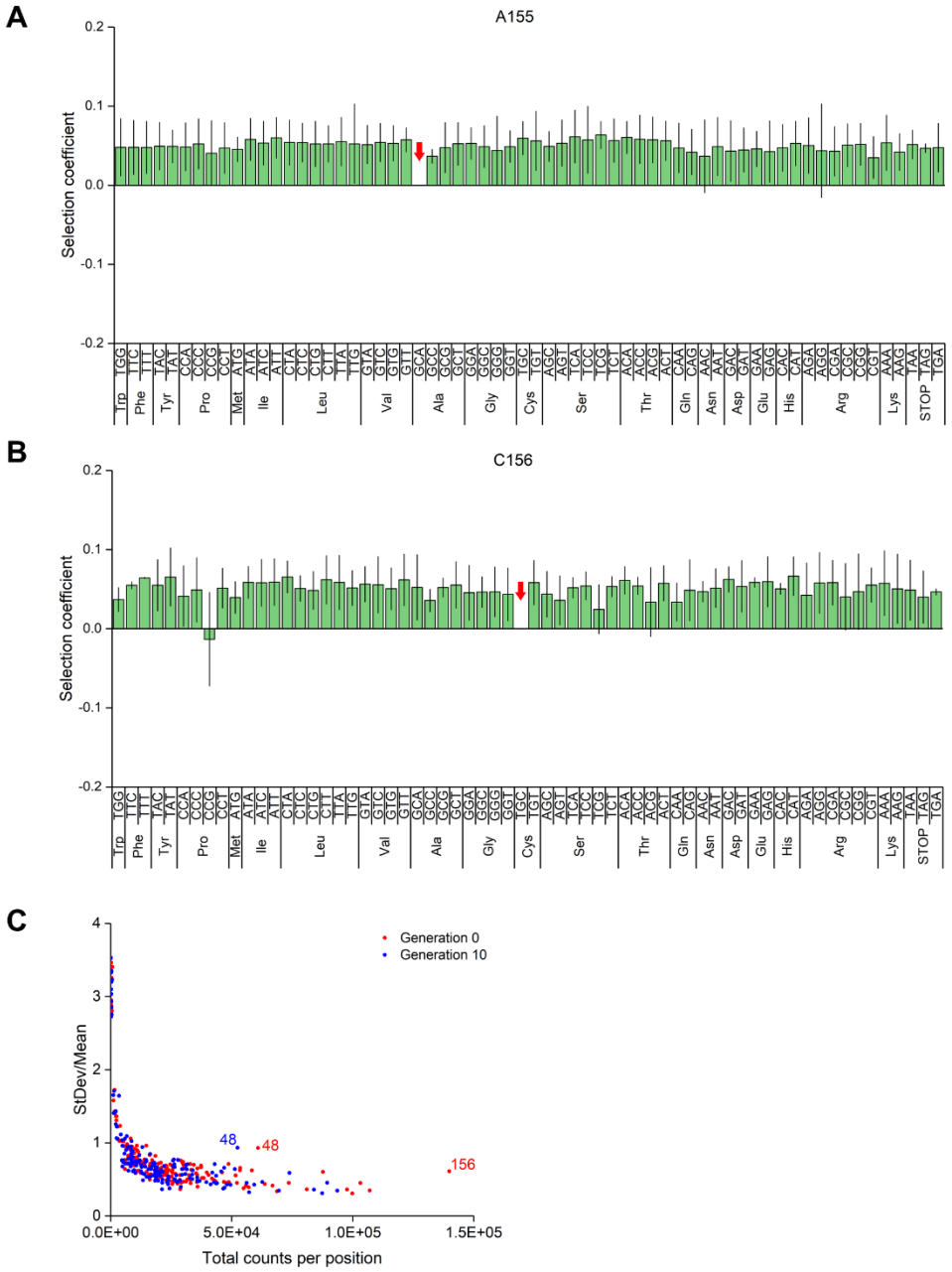

Figure S4. Artifactual beneficial fitness effects at residues 155 and 156 of AadB. Weighted mean collateral fitness effects of mutations in (**A**) A155 and (**B**) C156 as measured by two replica DMS growth competition experiments. Red arrow indicates wild-type codon. Error bars are 99% confidence intervals. (**C**) Plot of the standard deviation of all fitness measurements for nonsynonymous mutations at a specific residue divided by the mean fitness at that residue as a function of the total counts at the position. Data in red represents counts of a specific allele from before induction and data in blue represents counts of an allele after ten generations of growth.

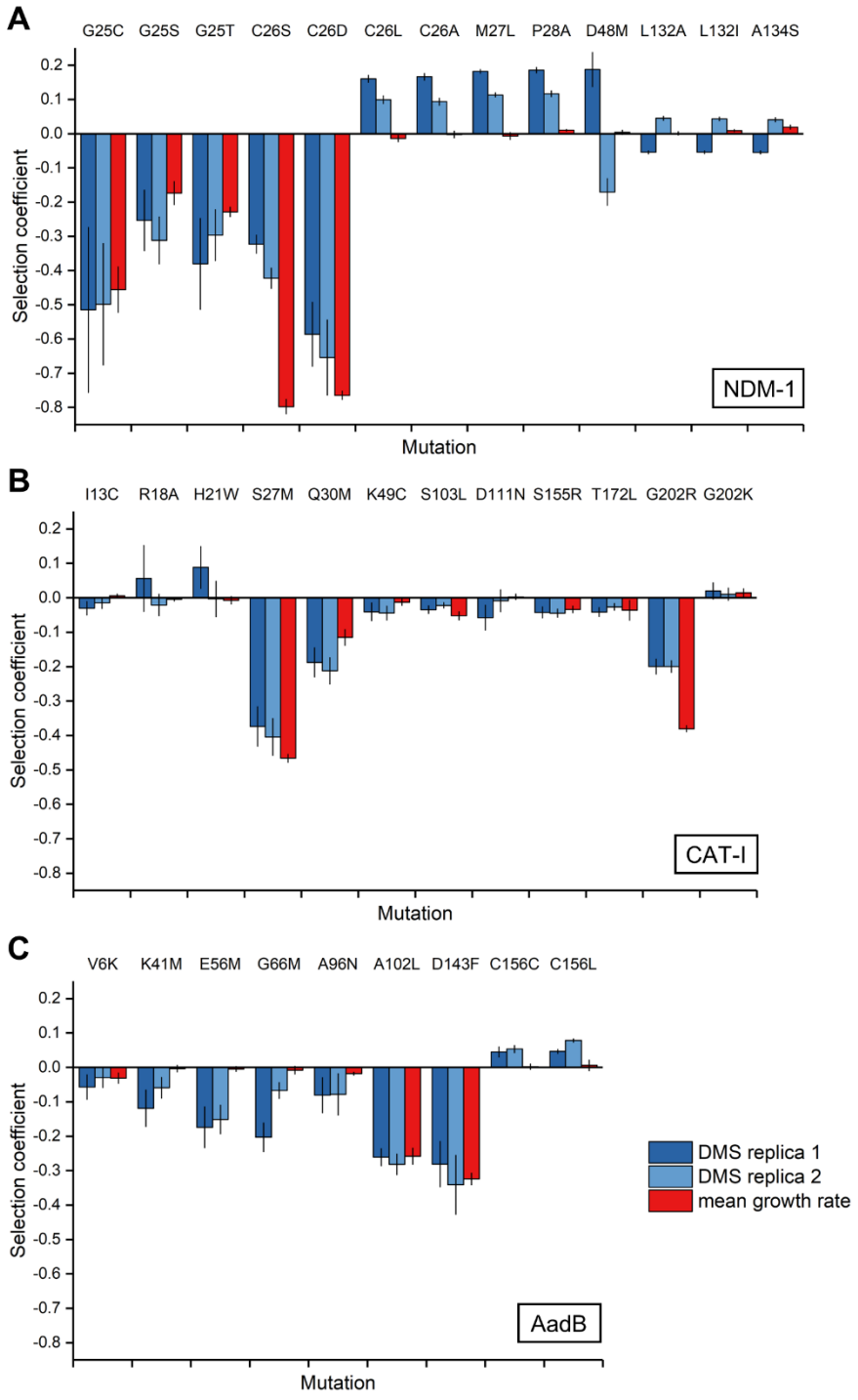

Figure S5. Confirmation of collateral fitness effects via monoculture growth. Selection coefficients for cells expressing mutations in (**A**) NDM-1, (**B**) CAT-I, and (**C**) AadB as measured by DMS (blue, two biological replicates) and mean growth rate over 6 h postinduction (red; n = 3). Mean growth rate was calculated from the starting and final OD (600 nm) for cells expressing wild-type and mutant versions of the antibiotic resistance proteins. Cells were grown in monoculture for 10 generations of wild-type growth. Error bars represent 99% confidence intervals. The C26S and C26D mutants of *NDM-1* contain synonymous mutations at L23 and S24 to eliminate the transposase insertion site. The C156C mutation in *aadB* is a synonymous mutation from TGC to TGT.

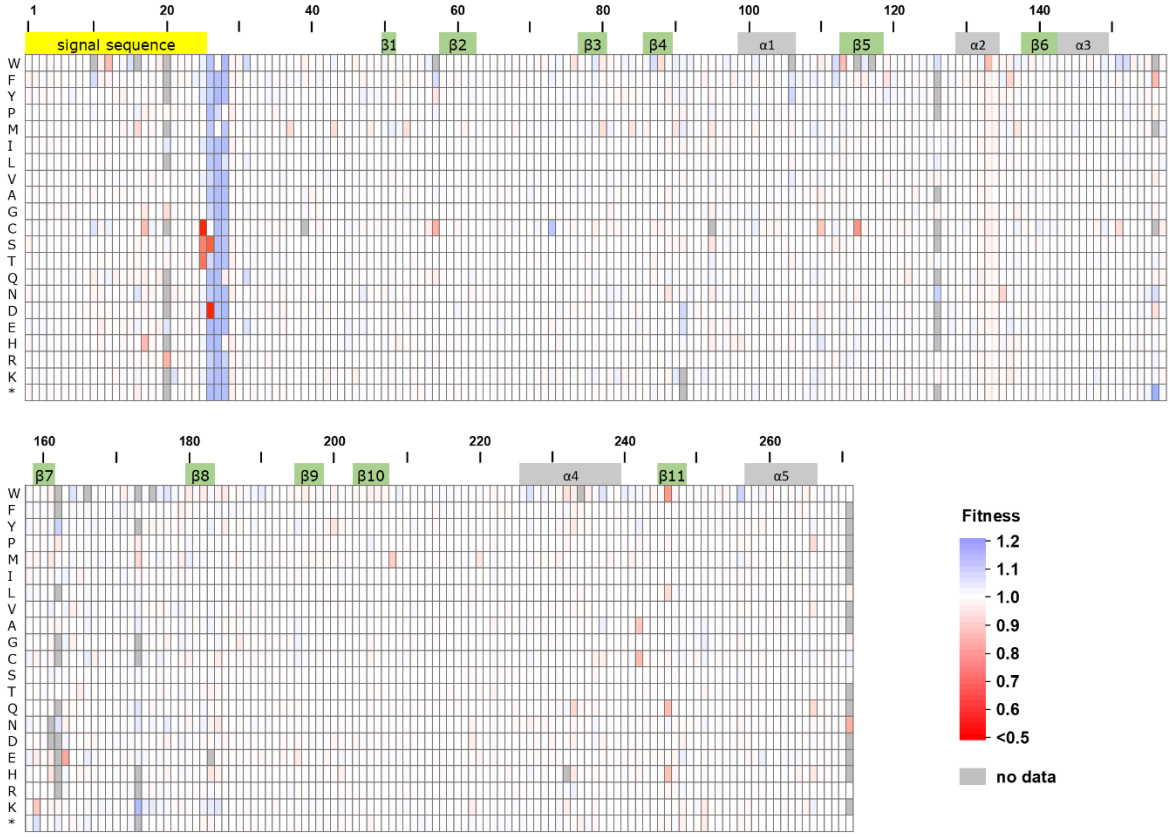

Figure S6. Weighted mean fitness measurements for NDM-1. Heat map of the weighted mean collateral fitness effects from two biological replicates of DMS in NDM-1. Cells expressing NDM-1 with the indicated missense or nonsense mutations were grown at 37°C for approximately 10 generations in LB media supplemented with 2.0% glucose and 1 mM IPTG. Mutations missing a fitness measurement in one or both replicates are shaded grey for no data. Regions corresponding to the signal sequence (yellow), α-helices (grey), and β-strands (green) are labeled along the top of the landscape. Tabulated fitness values are provided as **supplementary data S1**, Supplementary Material online.

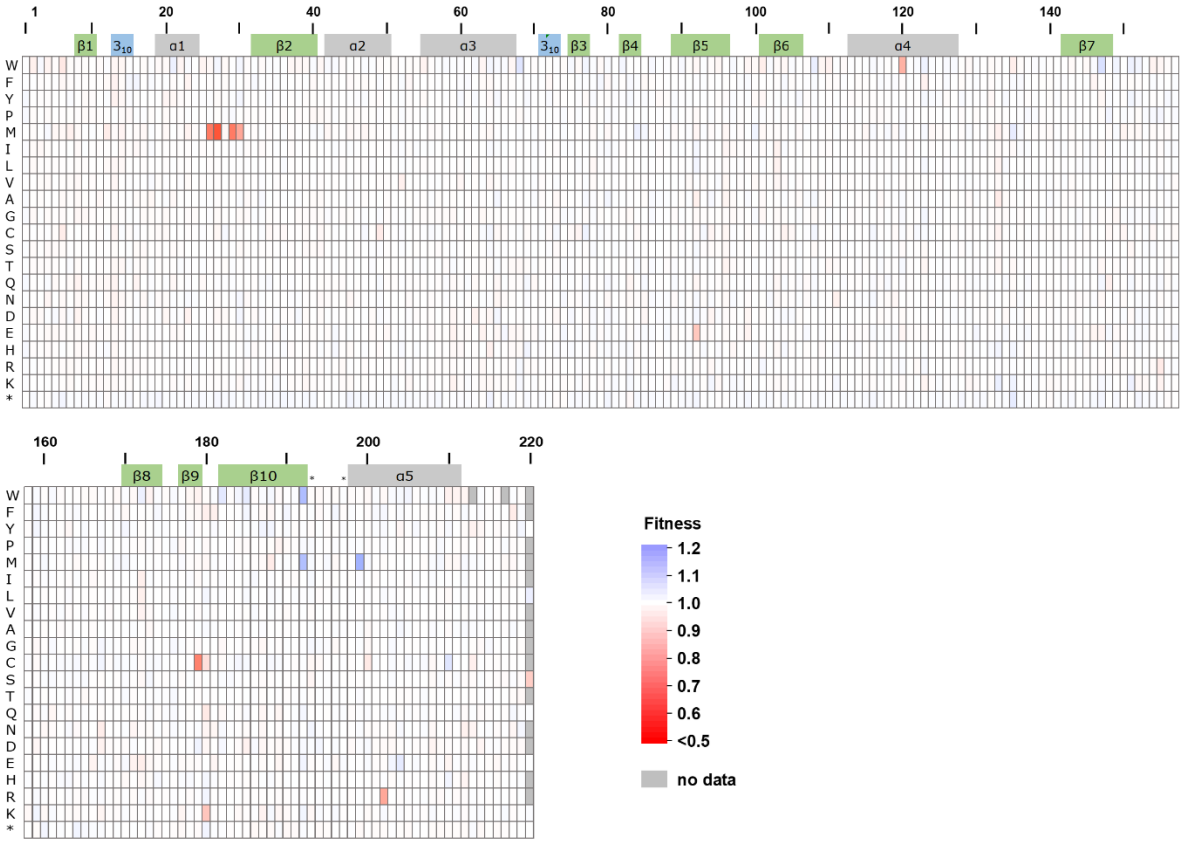

Figure S7. Weighted mean fitness measurements for CAT-I. Heat map of the weighted mean collateral fitness effects from two biological replicates of DMS in CAT-I. Cells expressing CAT-I with the indicated missense or nonsense mutations were grown at 37°C for approximately 10 generations in LB media supplemented with 2.0% glucose and 1 mM IPTG. Mutations missing a fitness measurement in one or both replicates are marked in grey. Regions corresponding to α-helices (grey), β-strands (green), 3_{10}-helices (blue), and key active site residues (*) are labeled along the top of the landscape. Tabulated fitness values are provided as **supplementary data S2**, Supplementary Material online.

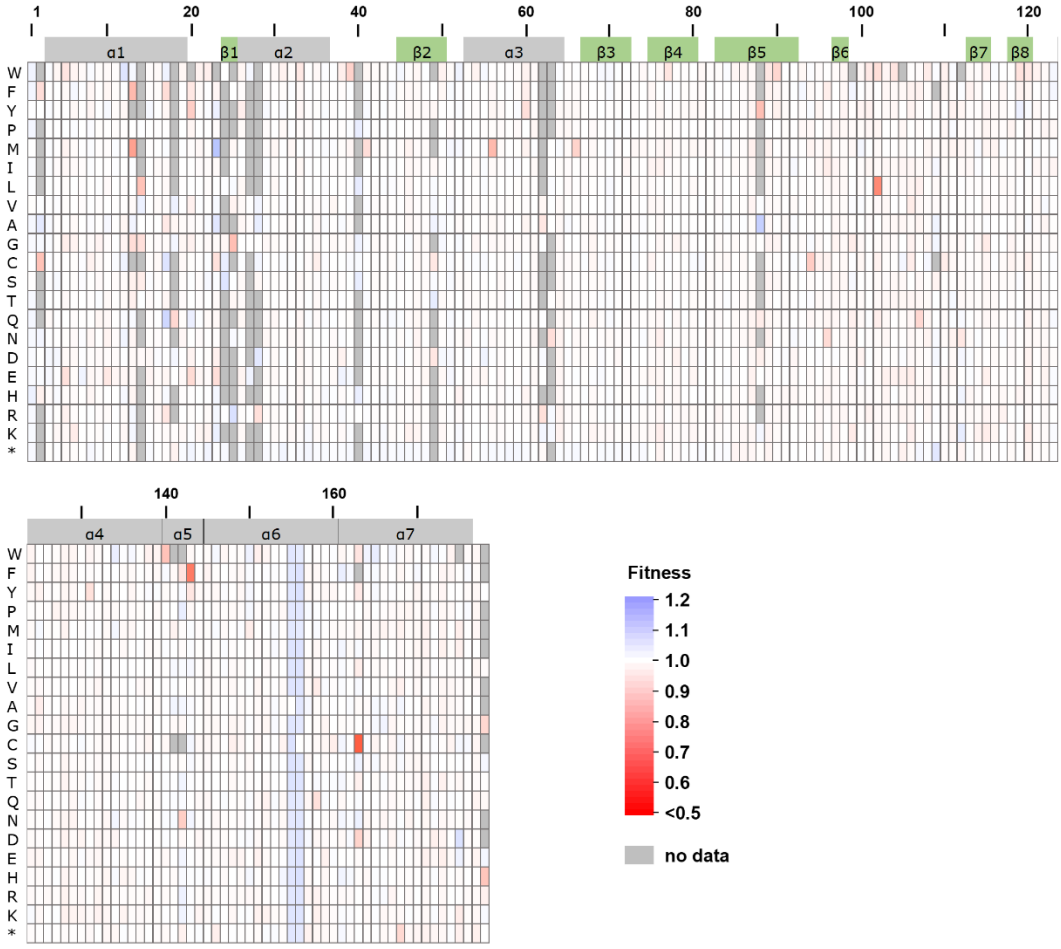

Figure S8. Weighted mean fitness measurements for AadB. Heat map of the weighted mean collateral fitness effects from two biological replicates of DMS in AadB. Cells expressing AadB with the indicated missense or nonsense mutations were grown at 37°C for approximately 10 generations in LB media supplemented with 2.0% glucose and 1 mM IPTG. Mutations missing a fitness measurement in one or both replicates are marked in grey. Regions corresponding to α-helices (grey) and β-strands (green) are labeled along the top of the landscape. Tabulated fitness values are provided as **supplementary data S3**, Supplementary Material online.

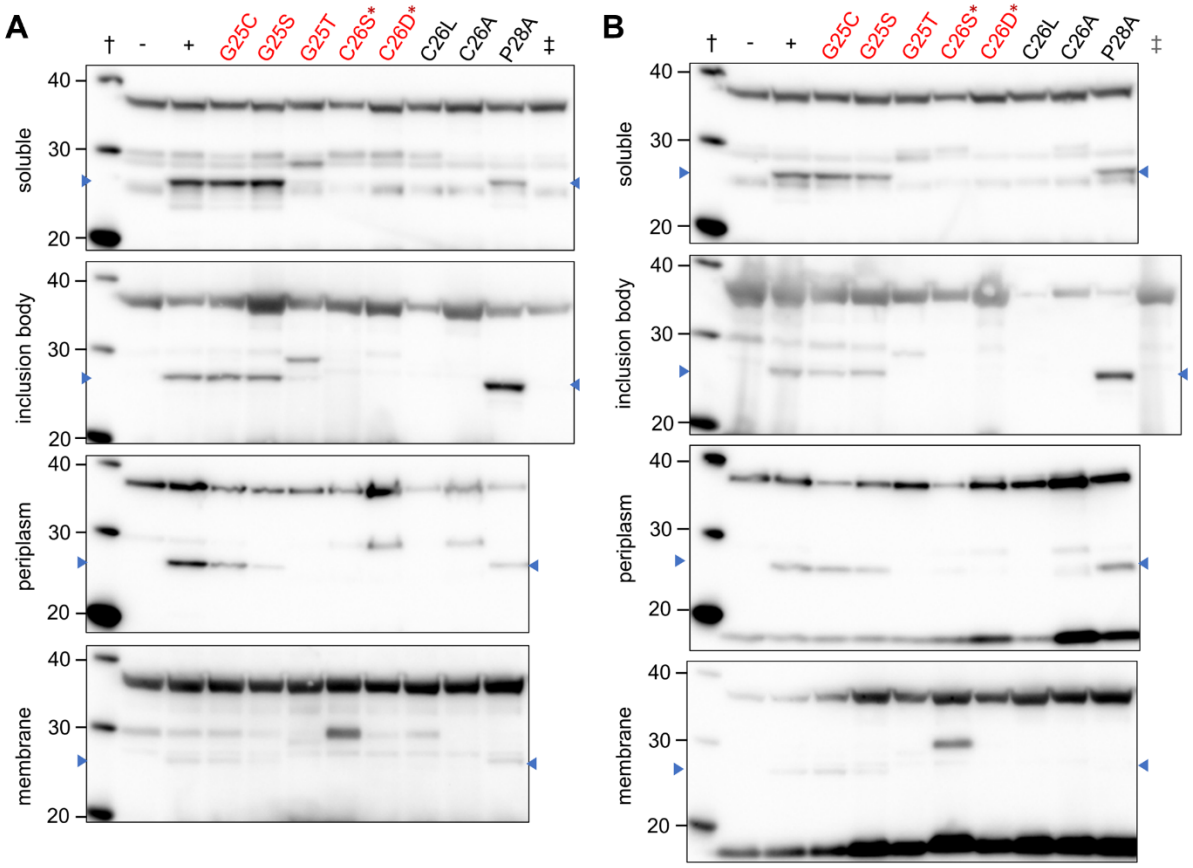

Figure S9. Western blots of fractionated cells expressing mutants of NDM-1. Cells expressing NDM-1 over six hours of induced growth were harvested, lysed, and fractionated into total soluble, inclusion body, periplasmic, and membrane fractions. Western blots for the (**A**) first and (**B**) second biological replicate are shown with deleterious mutations labeled in red and neutral mutations labeled in black. Samples from fractionated cells without induction of wild-type NDM-1 (-) and cells expressing wild-type NDM-1 (+) are included on the left of each blot along with the molecular weight standard (†). The C26S and C26D mutants include two synonymous mutations to prevent a transposase insertion indicated by (*). *CAT-I* samples (‡) corresponding to the respective fraction were included on Western blots to identify bands for *E. coli* proteins cross-reacting with the anti-NDM-1 antibodies.

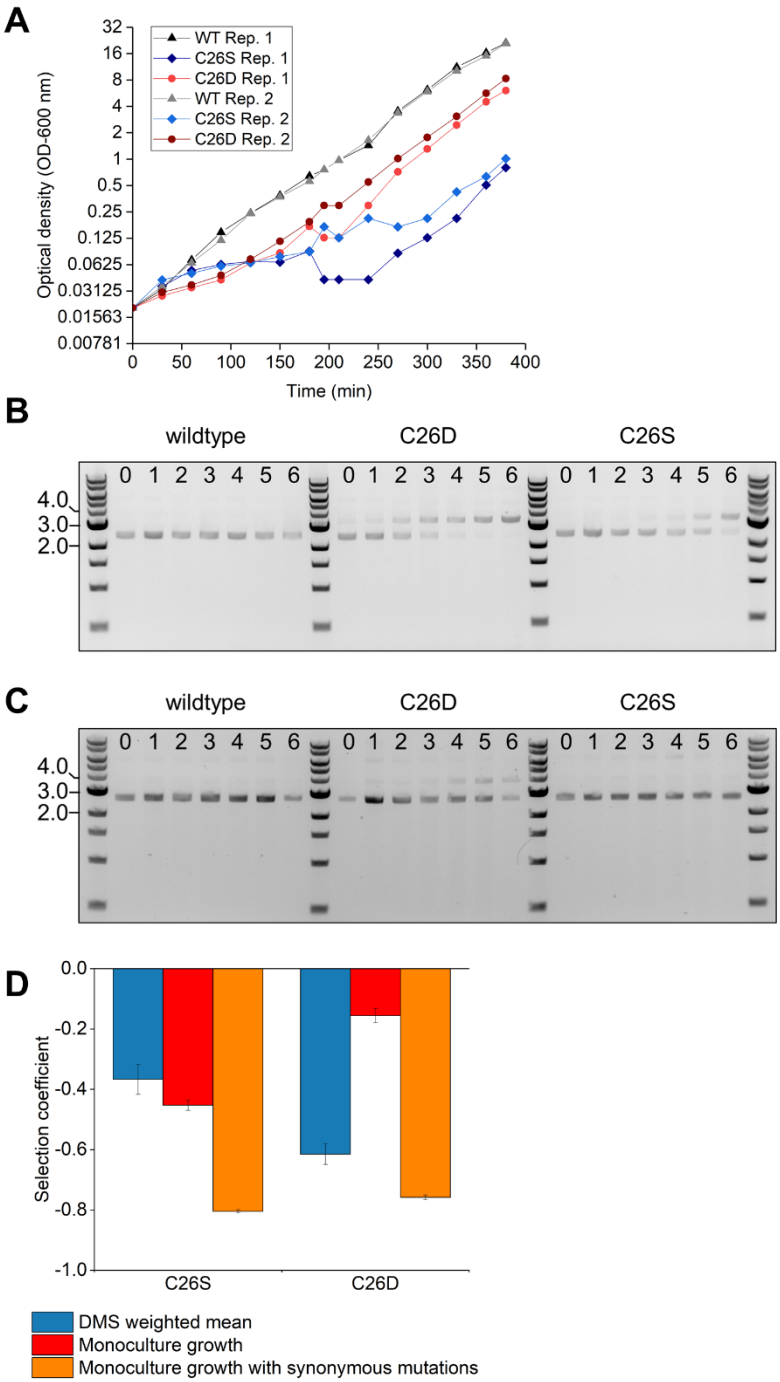

Figure S10. Correction for transposase insertion in NDM-1. (**A**) Initial monoculture growth experiments for C26D and C26S mutants were characterized by an initial phase after induction at time zero when growth rate slows followed by a later phase when growth rate accelerates. The acceleration happened sooner for C26D than for C26S. Sequencing of the DNA at the end of the experiment revealed insertion of an IS4-like element ISVsa5 family transposase during the induced growth phase. We collected plasmid extract from every hour of a six-hour induced growth phase to determine the timescale for the transposase insertion in (**B**) cells expressing the C26D and C26S mutants of *NDM-1* and in (**C**) cells expressing the same mutants but with synonymous mutations at L23 and S24 to disrupt the transposase insertion target site. Gels show supercoiled DNA. The lower band represents the pSKunk-1-

NDM-1 plasmid while the upper band develops after the transposase insertion occurs. Numbering along the top indicates the hour in the growth experiment from which the DNA was collected. (**D**) Comparison of the selection coefficient for cells with the C26S and C26D mutations as measured by DMS (blue) and monoculture growth (red and orange). The orange represents cells that also have the synonymous mutations at L23 and S24.

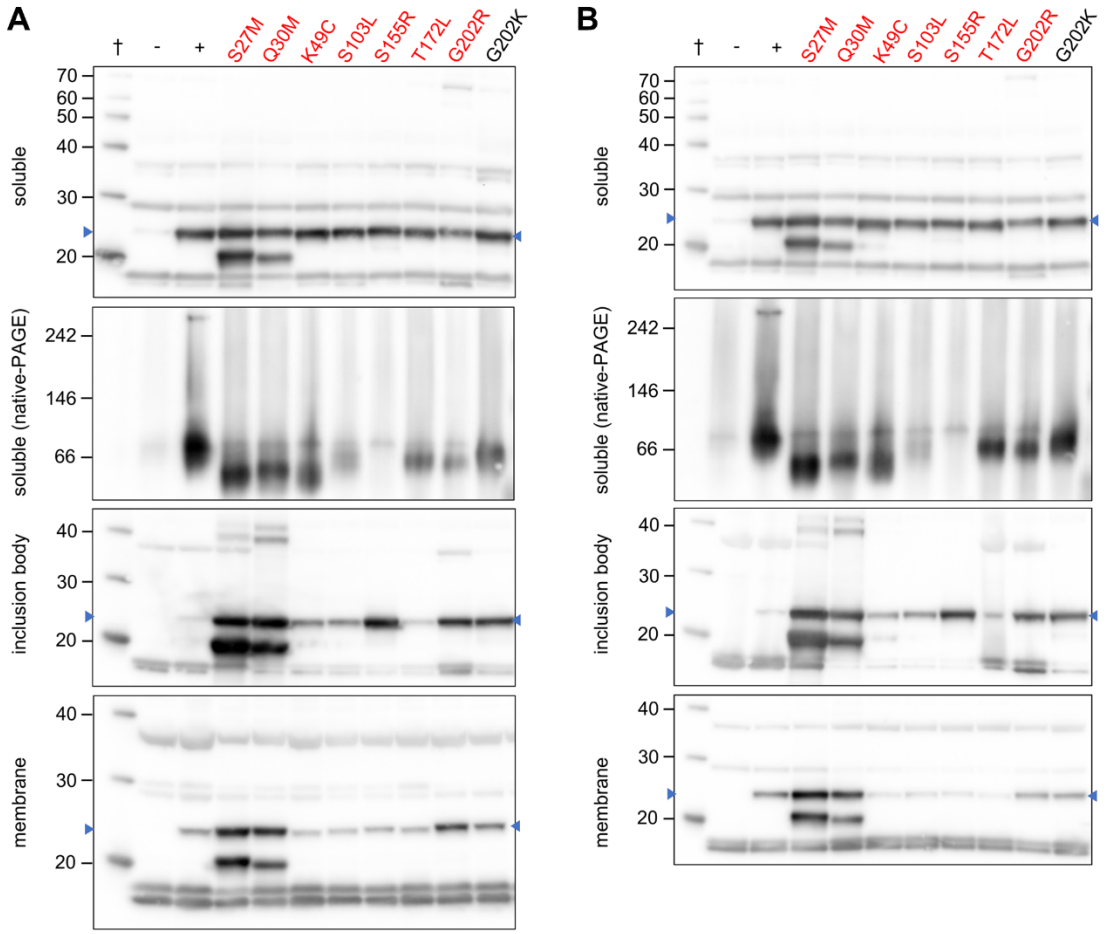

Figure S11. Western blots of fractionated cells expressing mutants of CAT-I. Cells expressing CAT-I over six hours of induced growth were harvested, lysed, and fractionated into total soluble, inclusion body, and membrane fractions. Western blots for the (**A**) first and (**B**) second biological replicate are shown with deleterious mutations labeled in red and neutral mutations labeled in black. Samples from fractionated cells without induction of wild-type CAT-I (-) and cells expressing wild-type CAT-I (+) are included on the left of each blot along with the molecular weight standard (†).

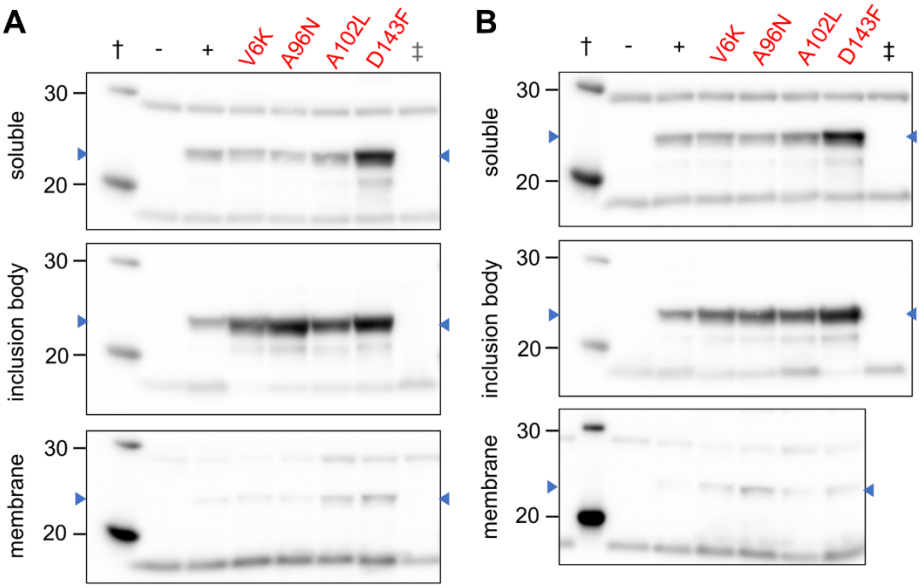

Figure S12. Western blots of fractionated cells expressing mutants of AadB. Cells expressing AadB over six hours of induced growth were harvested, lysed, and fractionated into total soluble, inclusion body, and membrane fractions. Western blots for the (**A**) first and (**B**) second biological replicate are shown with deleterious mutations labeled in red and neutral mutations labeled in black. Samples from fractionated cells without induction of wild-type AadB (-) and cells expressing wild-type AadB (+) are included on the left of each blot along with the molecular weight standard (†). CAT-I samples (‡) corresponding to the respective fraction were included on Western blots to identify bands for *E. coli* proteins cross-reacting with the anti-AadB antibodies.

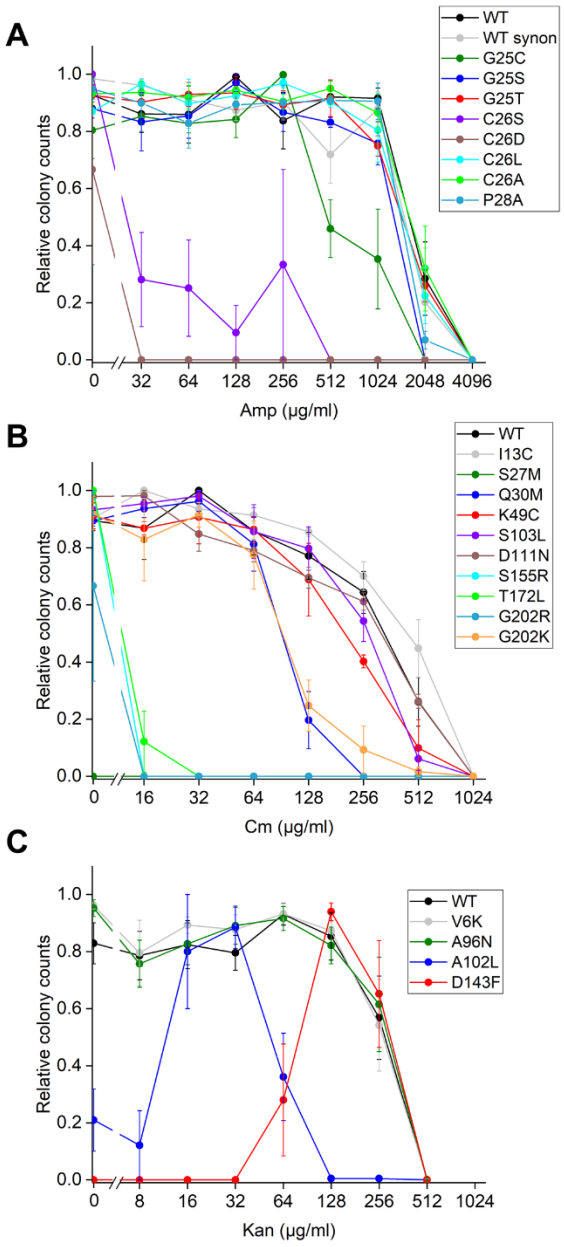

Figure S13. Relative colony counts for MIC assay. Relative colony counts for cells expressing wild-type or mutants of (**A**) *NDM-1* plated on ampicillin-containing plates, (**B**) *CAT-I* plated on chloramphenicol-containing plates, and (**C**) *aadB* plated on kanamycin-containing plates. Relative colony counts were calculated from the number of colony forming units (CFU) on a plate divided by the maximum number of CFU at any antibiotic concentration for that same variant. The resulting values were plotted as the mean with error bars representing the standard error of the mean (n = 3 for *NDM-1* and *CAT-I*; n = 5 for *aadB*). Expression of C26S and C26D of NDM-1 along with S27M of CAT-I were lethal in one or more replicates of the MIC assay as no colonies formed on plates lacking the corresponding antibiotic after overnight incubation with the IPTG inducer. Tabulated colony counts are provided as **supplementary data S5**, Supplementary Material online.

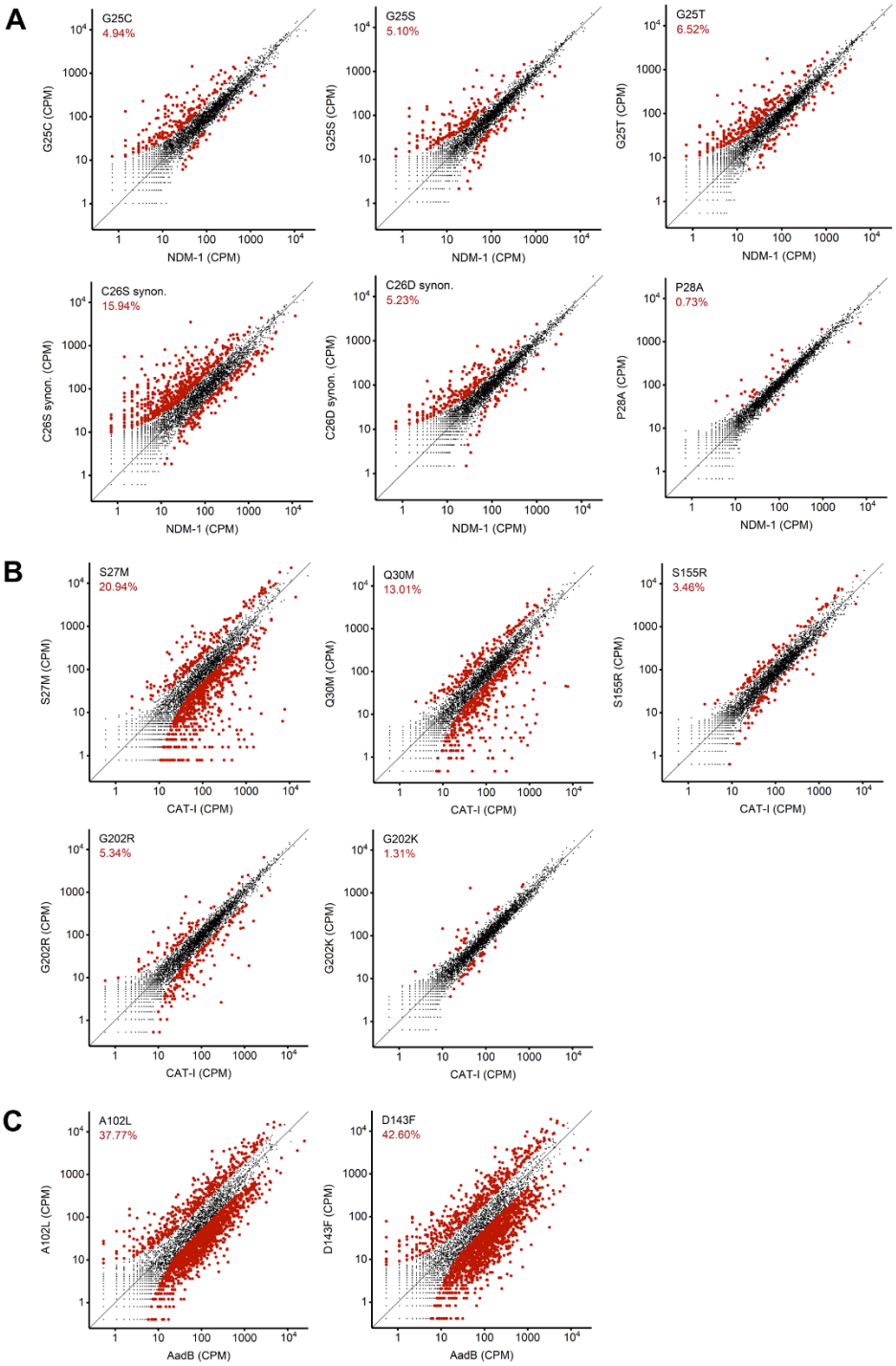

Figure S14. Differential gene expression caused by missense mutations. RNA-Seq results showing the gene expression levels in *E. coli* cells expressing a mutant relative to cells expressing the wild-type protein across mutations in (**A**) *NDM-1* (**B**) *CAT-I*, and (**C**) *aadB*. Data indicated with a larger, red circle represents genes in which expression changed by more than twofold with $P<0.001$ significance (Z-test) relative to wild-type. The percentage of genes which meet these criteria is indicated as a percentage in red on each plot. CPM, counts per million.

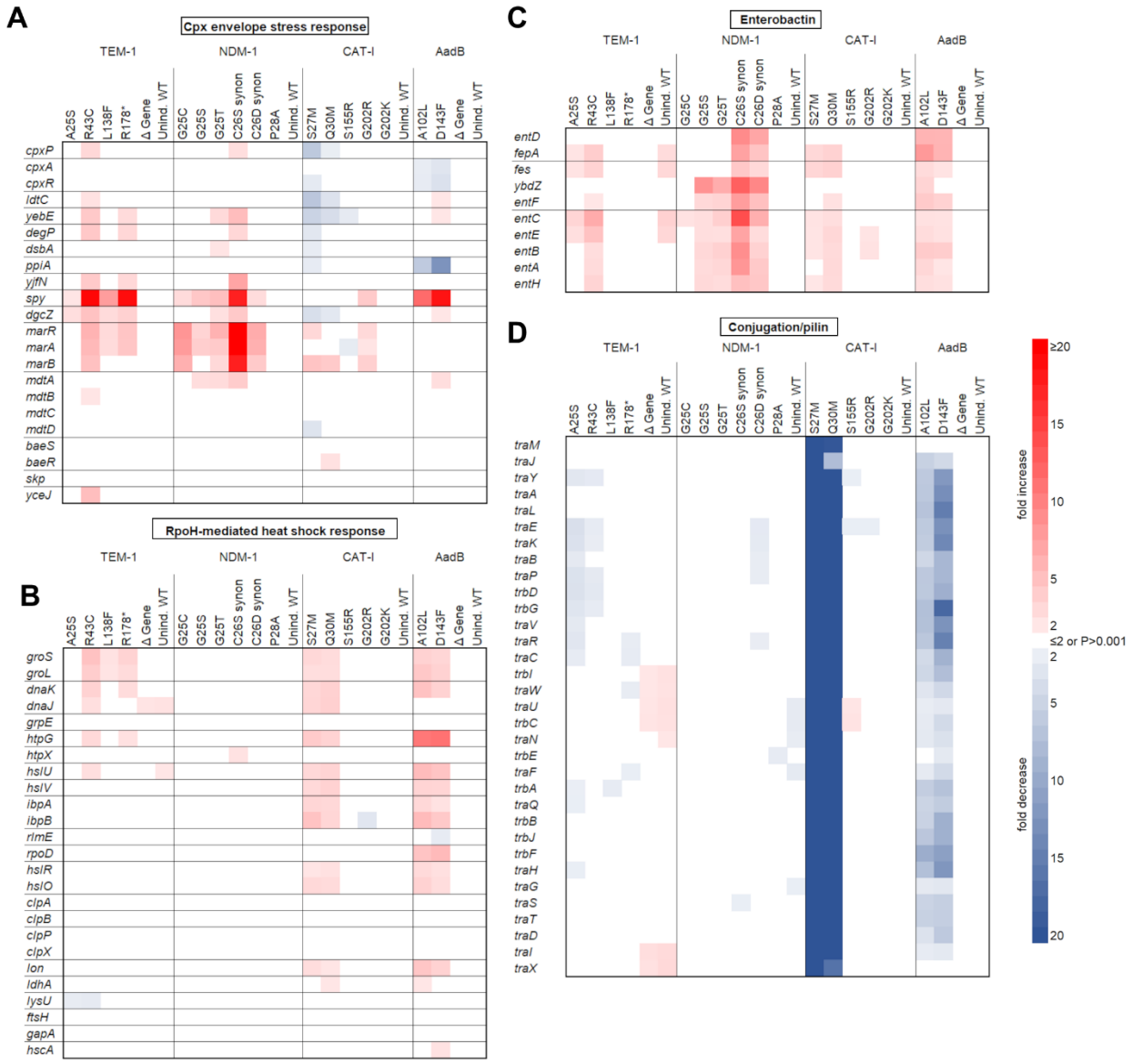

Figure S15. Effect of mutations related to stress responses and episome. RNA-Seq experiments revealed differential gene expression for genes corresponding to (**A**) the Cpx envelope stress response, (**B**) the σ^H-mediated heat stress response, (**C**) enterobactin biosynthesis, (**D**) and conjugation. Heat maps show genes that differed by greater than twofold expression and $P<0.001$ (Z-test) relative to cells expressing the wild-type antibiotic resistance genes. Control samples include ones in which wildtype gene expression was not induced (Unind. WT) and induced ones which lack the gene (Δ Gene).

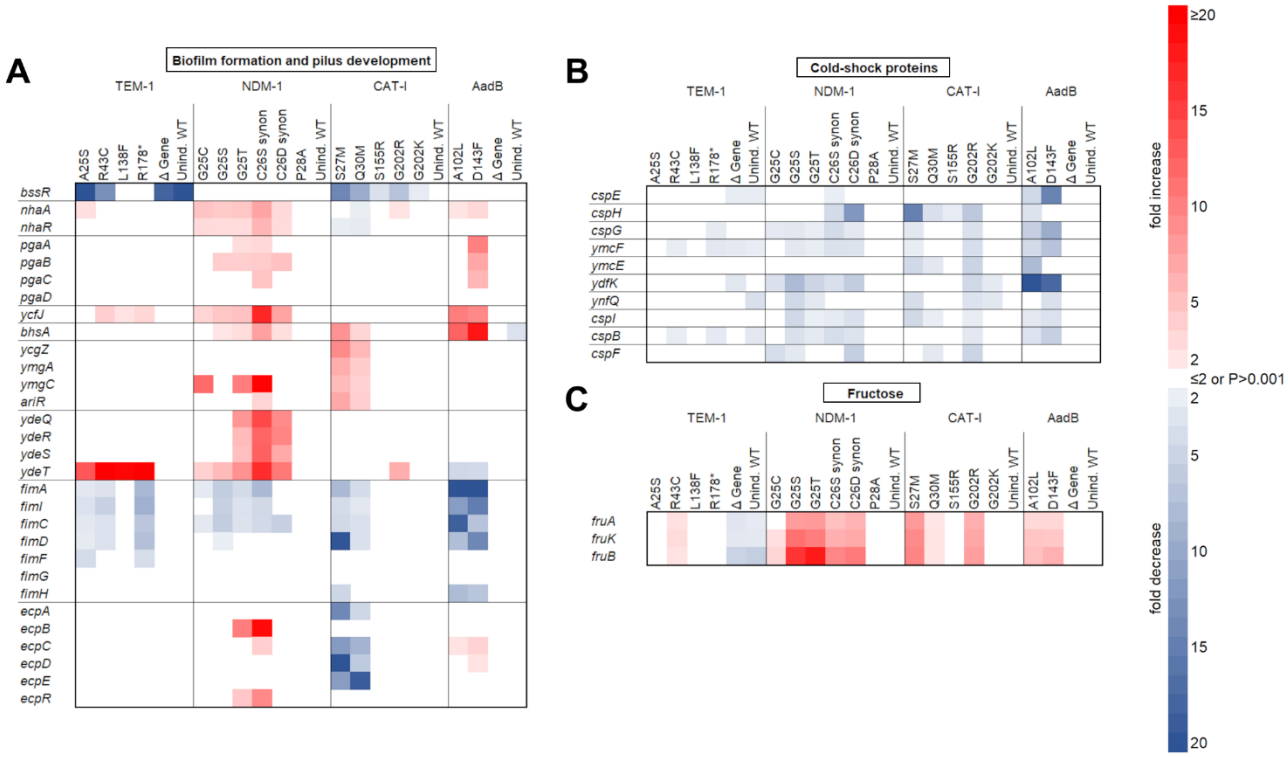

Figure S16. Effect of mutations on noted operons and pathways. We identified additional operons and pathways in which multiple genes were differentially expressed relative to their level in cells expressing the wild-type form of the antibiotic resistance gene. Heat maps for select genes belonging to (**A**) biofilm formation and pilus development, (**B**) the cold-shock response, and (**C**) the fructose catabolic process that differed by greater than twofold expression and $P<0.001$ (Z-test) relative to cells expressing the wild-type antibiotic resistance genes. Control samples include ones in which wildtype gene expression was not induced (Unind. WT) and induced ones which lack the gene (Δ Gene).

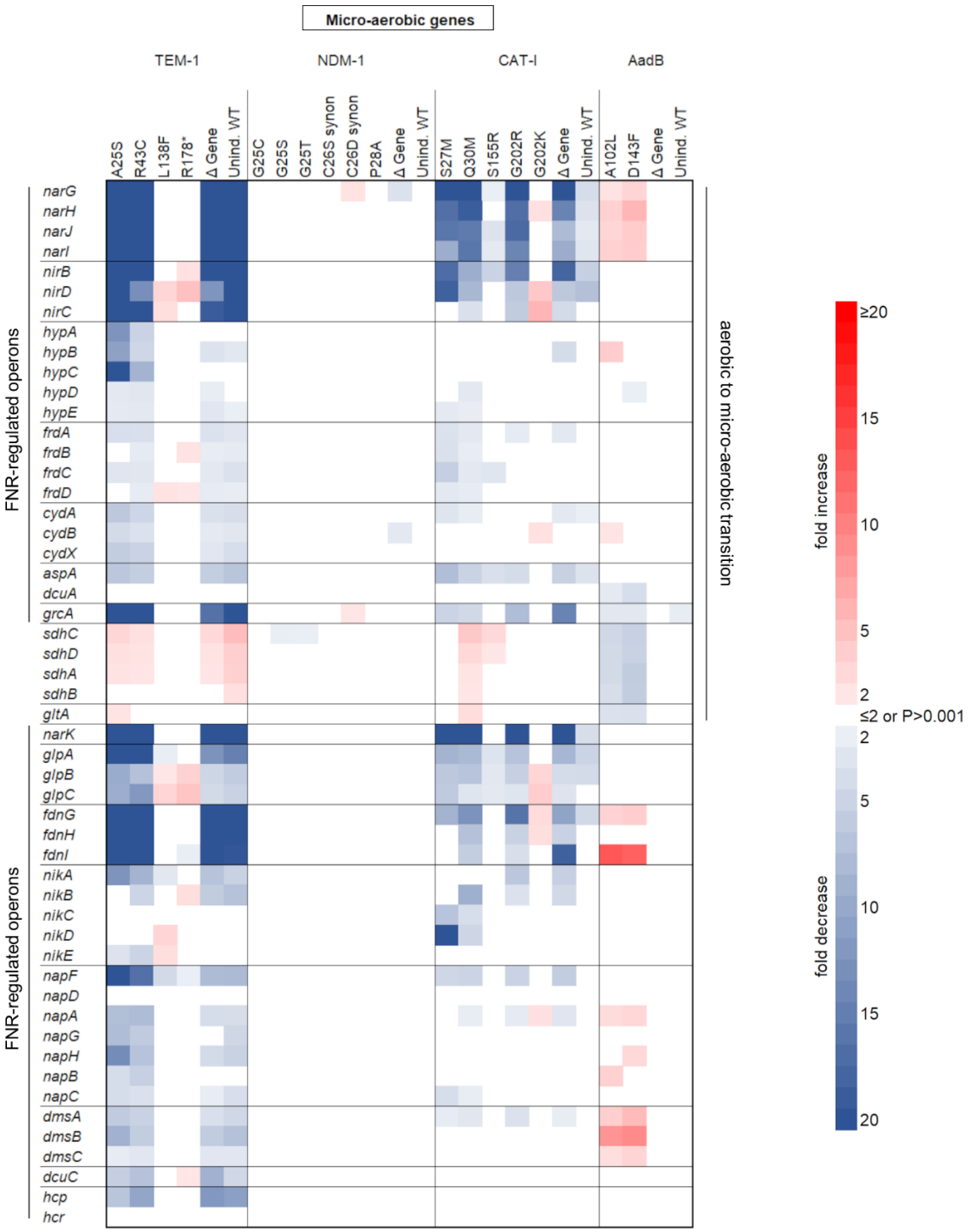

Figure S17. Differential expression of select genes involved in anaerobic growth. From RNA-Seq experiments, we also identified a set of genes corresponding to the transition from aerobic to micro-aerobic or anaerobic growth. Heat maps show fold-difference of twofold or more (*P*<0.001, Z-test) in gene expression relative to cells expressing the wild-type form of the antibiotic resistance protein. Genes belonging to operons regulated by FNR are identified along the left (Constantinidou et al. 2006). Genes associated with the transition from aerobic to micro-aerobic growth conditions are labeled on the right (Partridge et al. 2007).

Table S1. Translation initiation rates from methionine substitution in *CAT-I* as predicted by an algorithm described in Reis *et al*. (Reis and Salis 2020). The corresponding weighted mean collateral fitness effect measured by our two replicates of DMS is shown alongside with a white-red gradient to indicate the magnitude of the deleterious fitness effects.

	Translation Initiation Rate (au)	Fitness
WT start codon (M1)	558	1.000
F22M	33	0.997
E23M	704	0.975
A24M	85	0.995
F25M	63	1.005
Q26M	1467	0.697
S27M	811	0.610
V28M	124	0.986
A29M	1212	0.697
Q30M	432	0.799
C31M	30	0.997
T32M	38	0.995
Y33M	29	1.004
N34M	19	0.995

Table S2. Minimum inhibitory concentration (MIC) values in each replicate of the MIC assay[a].

	Sample	MIC Replicate 1 (µg/ml)	MIC Replicate 2 (µg/ml)	MIC Replicate 3 (µg/ml)	MIC Replicate 4 (µg/ml)	MIC Replicate 5 (µg/ml)
NDM-1	WT	4096	4096	4096	-	-
	WT (synon.)	2048	4096	2048	-	-
	G25C	2048	2048	1024	-	-
	G25S	2048	2048	2048	-	-
	G25T	4096	4096	4096	-	-
	C26S	0	0	0	-	-
	C26D	0	0	0	-	-
	C26L	4096	2048	4096	-	-
	C26A	4096	4096	4096	-	-
	P28A	2048	2048	4096	-	-
CAT-I	WT	1024	1024	1024	-	-
	I13C	1024	1024	1024	-	-
	S27M	0	0	0	-	-
	Q30M	128	256	256	-	-
	K49C	512	1024	512	-	-
	S103L	512	1024	512	-	-
	D111N	1024	1024	1024	-	-
	S155R	≤16	≤16	≤16	-	-
	T172L	≤16	≤16	32	-	-
	G202R	≤16	≤16	0	-	-
	G202K	256	512	256	-	-
AadB	WT	512	512	512	256	512
	V6K	512	512	512	256	512
	A96N	512	512	512	256	512
	A102L	128	64	128	64	128
	D143F	512	512	512	256	512

[a] The antibiotics used were ampicillin (*NDM*-1), chloramphenicol (*CAT*-I), and kanamycin (*aadB*). The C26S, C26D, and WT (synon.) samples also contain the synonymous mutations at L23 and S24 that disrupt the transposase insertion target site. The lowest chloramphenicol concentration tested was 16 µg/ml.

Supplementary References

Constantinidou C, Hobman JL, Griffiths L, Patel MD, Penn CW, Cole JA, Overton TW. 2006. A reassessment of the FNR regulon and transcriptomic analysis of the effects of nitrate, nitrite, NarXL, and NarQP as Escherichia coli K12 adapts from aerobic to anaerobic growth. *J. Biol. Chem.* 281:4802–4815.

Kram KE, Henderson AL, Finkel SE. 2020. Escherichia coli has a unique transcriptional program in long-term stationary phase allowing identification of genes important for survival. *mSystems* 5.

Partridge JD, Roberts RE, Poole RK. 2007. Transition of Escherichia coli from Aerobic to Micro-aerobic Regulatory Components involves fast and slow reacting regulatory components. *J. Biol. Chem.* 282:11230-11237.

Reis AC, Salis HM. 2020. An automated model test system for systematic development and improvement of gene expression models. *ACS Synth. Biol.* 9:3145–3156.

Captions for data files

Data S1. Excel file for DMS sequencing counts, fitness values, and associated statistics for collateral fitness effects in NDM-1.

Data S2. Excel file for DMS sequencing counts, fitness values, and associated statistics for collateral fitness effects in CAT-I.

Data S3. Excel file for DMS sequencing counts, fitness values, and associated statistics for collateral fitness effects in AadB.

Data S4. Excel file for RNA-seq sequencing counts, fold-difference in expression, and associated statistics.

Data S5. Excel file for NDM-1, CAT-I, and AadB MIC assay colony counts.